REPORT DOCUMENTATION PAGE

Form Approved
OMB No. 0704-0188

1. REPORT DATE: 03-03-2006	2. REPORT TYPE: Final Technical Report	3. DATES COVERED: 01/05-12/05
4. TITLE AND SUBTITLE: Quiet Tunnel Experiments of Shock/Boundary Layer Interactions		5a. CONTRACT NUMBER: FA9550-05-1-0178 5b. GRANT NUMBER: N/A 5c. PROGRAM ELEMENT NUMBER: N/A
6. AUTHOR(S) : Chokani, Ndaona		5d. PROJECT NUMBER: N/A 5e. TASK NUMBER: N/A 5f. WORK UNIT NUMBER: N/A
7. PERFORMING ORGANIZATION NAME(S) AND ADDRESS(ES) Duke University, Office of Sponsored Programs 705 Broad Street, Box 90941 Durham NC 27708-0491		8. PERFORMING ORGANIZATION REPORT NUMBER: N/A
9. SPONSORING / MONITORING AGENCY NAME(S) AND ADDRESS(ES): AFOSR/NA AFOSR 875 N Randolph St Arlington VA 22203 Dr John Schmisseur/NA		10. SPONSOR/MONITOR'S ACRONYM: AFOSR 11. SPONSOR/MONITOR'S REPORT NUMBER: N/A

12. DISTRIBUTION / AVAILABILITY STATEMENT: Approved for public release. Distribution unlimited.

Approved for public release,
distribution unlimited

AFRL-SR-AR-TR-06-0452

13. SUPPLEMENTARY NOTES

14. ABSTRACT:
The effect of freestream noise on the shockwave/turbulent boundary layer interaction on a compression ramp is experimentally examined. The experiments are conducted in a supersonic low-disturbance tunnel under both low-level ("quiet") and high-level ("noisy"/"conventional") freestream noise levels. A large-scale, low-frequency oscillation of the shock, that is comparable to that measured in previous conventional tunnel experiments is observed. The intermittent length of the interaction is comparable to that of previous experiments, but larger than that predicted in numerical simulations. Thus the freestream noise levels do not appear to be the source of the previously reported discrepancies between conventional tunnel experiments and simulations.

15. SUBJECT TERMS: shockwave/boundary layer interaction. turbulent boundary layer. supersonic flow.

16. SECURITY CLASSIFICATION OF:			17. LIMITATION OF ABSTRACT: none	18. NUMBER OF PAGES	19a. RESPONSIBLE PERSON: N. Chokani
a. REPORT: unlimited	b. ABSTRACT: unlimited	c. THIS PAGE: unlimited		92	19b. TELEPHONE No: (919) 660-5310

Contents

List of Figures

List of Tables

Nomenclature

Latin letters

a	half height of dark cut-off gridlines in focusing schlieren
b	height of clear cut-off gridlines in focusing schlieren
a_w	hot-wire overheat ratio: $a_w = \dfrac{R_w - R_a}{R_a}$
A	imaging lens aperture in focusing schlieren system
A, B	constants in hot-wire calibration law
c_f	friction coefficient
DU	depth of unsharp focus
E	output voltage
F	field of view
f	frequency
H	form parameter $H = \delta_1/\theta$
H_i	incompressible form parameter (see eq. 3.1)
L, l, L', l'	parameters of focusing schlieren system
L_i	intermittent length
L_{ui}	upstream interaction length
M	Mach number
n	constant in hot-wire calibration law, number of gridlines per mm in focusing schlieren system
m	focusing schlieren magnification
p	static pressure
p_0	stagnation pressure
p_t	total pressure

R	unit Reynolds number, perfect gas constant
Re	Reynolds number
t	time
$S_{\rho u}$	hot-wire nondimensional sensitivity to mass flow
T	static temperature
T_0	total temperature
U, u	velocity component parallel to the probe axis (x-component)
x, y, z	coordinate system
w	resolution of focusing schlieren system

Greek letters

δ	boundary layer thickness
δ_1	boundary layer displacement thickness
θ	boundary layer momentum thickness
ϵ	focusing schlieren resolution
λ	wavelength of light
γ	ratio of specific heats (1.4), intermittency
ρ	density

Acronyms

AC	alternative current
bvc	bleed valves closed
bvo	bleed valves open
BVC	bleed valves closed
BVO	bleed valves open
CTA	constant temperature anemometer
DC	direct current
DNS	direct numerical simulation
$LaRC$	Langley Research Center

LES	large eddy simulation
NASA	National Aeronautics and Space Administration
PSD	power spectral density
RANS	Reynolds-Averaged Navier Stokes
RMS	root mean square
SLDT	supersonic low disturbance tunnel
STBLI	shockwave/turbulent boundary layer interaction

Subscripts

bvc	bleed valves closed
bvo	bleed valves open
e	free-stream, edge of boundary layer
0	stagnation
rms	root mean square
mean	mean

Acknowledgements

This report was prepared in conjunction with Julien L. Weiss, postdoctoral research assistant on the project; the author is grateful for this support.

The support of Fang-Jenq Chen, Rudolph A. King, Catherine B. McGinley, Hugh T. Pinkston, and Stephen P. Wilkinson of NASA LaRC during the conduct of the experiments is very much appreciated. The efforts at NASA LaRC of Meelan M. Choudhari, Susan A. Gorton, and William L. Sellers to provide access to the facilities in the Flow Physics and Control Branch are gratefully acknowledged.

The advice of Michael A. Kegerise and Leonard M. Weinstein of NASA LaRC in the design of the focusing schlieren system is also greatly appreciated.

The views and conclusions contained herein are those of the author and should not be interpreted as necessarily representing the official policies or endorsements, either expressed or implied, of the Air Force Office of Scientific Research or the U.S. Government.

Chapter 1

Introduction

Shockwave/turbulent boundary layer interactions (STBLI) are ubiquitous phenomena in high-speed flows that directly influence the lift, drag, propulsion efficiency, stability, control surface authority, peak thermo-mechanical loads, structural fatigue and life cycle costs on high-speed vehicles. Given the prevalence of the phenomenon, it is clear that an understanding of STBLIs is important for the design of high-speed vehicles. Despite the significant progress in our understanding of STBLI that has been made over the last decade, the prediction of STBLI using numerical methods is still far from satisfactory. For example, in compression ramp flows with high deflection angles, conventional Reynolds Averaged Navier-Stokes (RANS) models do not predict well either the location of the separation shock, the size of the separation region at the corner, nor the mean velocity profiles downstream of the shock [26]. Also other important design parameters such as skin friction, heat transfer, and fluctuating thermo-mechanical loads are poorly predicted [19].

One of the reasons cited for the poor predictions is the inherent unsteadiness of STBLI [9]. Indeed, a number of experimental studies show that the shock wave structure in different types of STBLIs is characterized by large-scale random shock oscillations (*e.g.* Dolling [11] and references therein). These oscillations produce the large fluctuating pressure loads at the wall. However Dolling [10] indicates that the mechanisms driving the shock oscil-

lations are still not well understood. Dynamic wall pressure measurements in shock-induced separated flows show that the STBLI is characterized by an intermittent zone in which the fluctuating wall pressure signal has contributions from three different flow components: the incoming turbulent boundary layer, the separated flow downstream of the shock, and the rapid rises and falls in pressure associated with the motion of the shock foot. This motion of the shock foot produces the largest contribution to the RMS wall pressure. The frequency of the shock foot's motion appears to be at least an order of magnitude lower than the boundary layer's characteristic frequency U/δ, where U is the free stream velocity and δ is the boundary layer thickness [11]. This relatively low frequency motion of the shock foot is observed in compression ramp, blunt fin, and cylinder-induced STBLIs [12]. Andreopoulos and Muck [3] conducted experiments on a Mach 3 compression ramp flow, and suggested that the frequency of the shock motion scales with the bursting frequency of the incoming turbulent boundary layer. This observation was, however, not confirmed by Thomas *et al* [30] whose experiments focused on the unsteady characteristics of STBLI. Erengil and Dolling [16] showed that there is a correlation between the wall pressure fluctuations beneath the incoming boundary layer and the velocity of the separation shock foot; they inferred that the small-scale motion of the shock is caused by its response to the passage of turbulent fluctuations through the interaction, whereas the large-scale motion is a result of the shock's displacement due to the expansion and contraction of the shock-induced separation bubble. Ünalmis and Dolling [31] studied the relationship between the motion of the separation shock and the Pitot pressure in the upstream turbulent boundary layer. Beresh *et al* [5, 18] used particle image velocimetry to correlate the velocity fluctuations in the incoming boundary layer with the fluctuating wall pressures. Although all these experiments shed some light on the possible mechanisms that play a role in the shock motion, there is still no comprehensive explanation of the physical causes of the unsteadiness.

Recent advances have enabled the computation of STBLI by means of Direct Numerical Simulation (DNS) and Large Eddy Simulation (LES). Rizzetta and Visbal [22] performed a LES of a Mach 3 compression ramp

interaction with different ramp angles. They compared their results to the experimental data of Dolling and Murphy [13] and found very different characteristics of the shock motion. The numerical simulation exhibited high frequency shock oscillations of similar magnitude to the characteristic frequency of the incoming boundary layer but did not show any large scale excursions of the shock. The large-scale/low-frequency motion observed in the experiments was not reproduced in the LES, nor in the DNS of Adams [1] or Wu and Martin [34]. This mismatch between numerical simulations and experimental results, as well as the absence of a clear correlation between the incoming boundary layer and the low frequency shock motion, has raised the speculation that the shock motion could be driven, at least in part, by some type of facility dependent forcing [10]. A common feature of the wind tunnels in which the STBLI experiments have been conducted to-date is the relatively high level of free stream disturbances that is present in the test section. In conventional high-speed wind tunnels, the test section disturbances are mainly due to the aerodynamic noise that is generated in the turbulent boundary layer on the nozzle walls and radiated, in the form of fluctuating Mach waves, into the free stream [20]. These fluctuating Mach waves interact with the model's boundary layer and can potentially affect its behavior. Only in the so-called quiet wind tunnels can the level of free-stream disturbances be reduced by maintaining the nozzle boundary layer laminar and thus reducing acoustic radiation into the test section [4].

The present work is the first experimental investigation of the structure of an unswept compression ramp interaction in a quiet wind tunnel. Measurements are performed in the Supersonic Low Disturbance Wind Tunnel (SLDT) at NASA Langley Research Center with a special emphasis on the shock unsteadiness. SLDT has the unique capability of being able to provide a very low disturbance environment in which the free-stream noise level is at least an order of magnitude lower than in conventional facilities. The tunnel can also be operated in a conventional mode, thus a parametric study of the effect of free-stream disturbances on the STBLI can be conducted. Furthermore, in the present work, the measurements are performed at a Reynolds number that is low enough to enable a comparison between the

present experiments and subsequent DNS/LES.

The report is organized as follows. In Chapter 2, the wind tunnel, compression ramp model, instrumentation, and data reduction techniques are described. The results of the experimental work are discussed in Chapter 3. The more complete details of the experimental results are presented in Appendices A - E. Chapter 4 presents the conclusions drawn from the present work.

Chapter 2

Experimental Method

2.1 The Supersonic Low Disturbance Tunnel

The present experiments are performed in the Mach 3.5 Supersonic Low Disturbance Tunnel (SLDT) at the NASA Langley Research Center. SLDT is a pressure-vacuum blowdown wind tunnel that has a virtually unlimited testing time due to the large air storage capacity that is available at NASA LaRC. In this tunnel, the nozzle boundary layer can be removed by bleed slots that are located just upstream of the nozzle throat. The boundary layer that develops downstream of the nozzle throat is therefore initially laminar. Since most of the free stream disturbances in supersonic tunnels are fluctuating Mach waves that are radiated from the turbulent boundary layer, this results in a portion of the test section - the so-called "quiet test core" - that is free from acoustic disturbances. The level of disturbances in the quiet test core is typically one order of magnitude lower than in the portion contaminated by acoustic radiation. The tunnel can also be run in a "noisy" mode by closing the bleed slots. In this case, the boundary layer on the nozzle is turbulent from immediately downstream of the throat and the disturbance levels in the test section are similar to those in a conventional facility. Therefore, operation of the tunnel with bleed valves open (BVO) or closed (BVC) (that is quiet or noisy conditions, respectively) readily provides a means to examine the effect of free-stream disturbances on STBLI. More

detailed information about SLDT are presented in Beckwith *et al* [4], Chen *et al* [7], and the references therein.

A schematic of SLDT's test section is shown in Fig. 2.1. The dimensions of the nozzle exit are 6″(vertical) × 10″ (horizontal) and the distance between the Mach rhombus tip and the nozzle exit plane is 10″. Optical access through the test section is provided through doors on the sidewall that are equipped with schlieren windows. The optically accessible region is from 3.25″ downstream of the nozzle exit plane up to the downstream end of the Mach rhombus. The nozzle blocks of SLDT were re-polished in FY2004 prior to the start of the present experiments. Therefore, the level of free-stream disturbances along the centerline of the test section are measured in the present work to verify the quiet operation of the tunnel. These measurements are discussed in section 3.1.

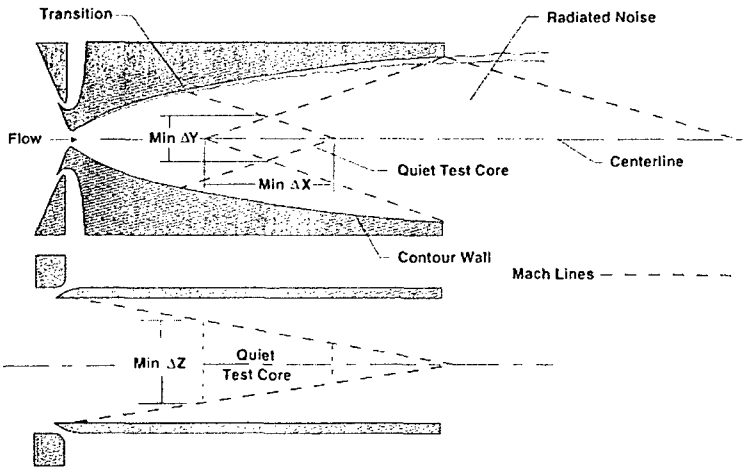

Figure 2.1: Schematic of the SLDT test section. Side view (top) and plan view (bottom)

2.2 Compression Ramp Model

The model is a 11.5″ × 7″ flat plate that is mounted horizontally on the centerline of the tunnel. A 24° wedge with a 1.5″ base is fixed at the aft end of the plate. The compression ramp corner is located 4″ downstream of the nozzle exit plane. The salient dimensions of the model are shown in Fig. 2.2.

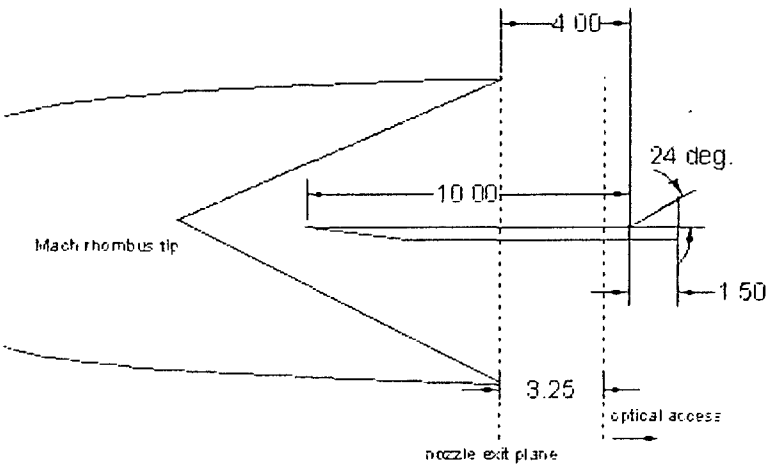

Figure 2.2: Sketch of compression ramp model, all dimensions in inch

The plate-ramp model is made from stainless steel, alloy SS 17-4 with the heat treatment H900. The model is attached to an existing sting/strut. The model dimensions are specified to meet the NASA LaRC wind-tunnel model criteria [6]. A picture of the model mounted on the sting/strut is shown in Fig. 2.3.

The flat plate is instrumented with four Entran EPIH 113-50psi miniature dynamic pressure transducers that are located upstream of the compression ramp. However, hardware problems were encountered during the course of the experiments and thus no data were obtained with the transducers.

A turbulator is used to generate a well developed turbulent boundary

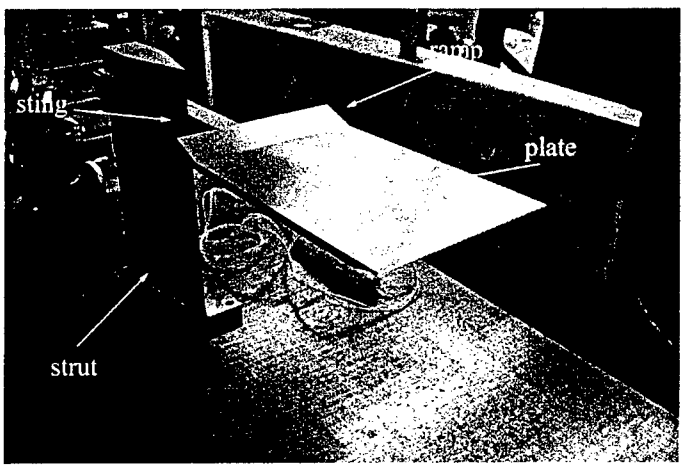

Figure 2.3: Compression ramp model mounted to the sting/strut

layer upstream of the ramp corner. Two different turbulators are used in the experiments. The first turbulator (subsequently referred to as *Turbulator 1*) is made of 3D roughness elements that are randomly distributed along a 0.25″ strip at the leading edge of the plate. The roughness elements are no. 120 silicon carbide grit that is glued, using radio cement, across the width of the plate. It was observed in the experiments that this turbulator did not generate a turbulent boundary layer under the low pressure ($\leq 50psi$), quiet flow conditions of SLDT. In order to generate a turbulent boundary layer under these conditions, a second turbulator (hereafter referred to as *Turbulator 2*) was made by gluing a 1.5″ wide strip of no. 40 sandpaper along the plate leading edge. This turbulator also extended across the width of the plate. Under quiet flow conditions and at stagnation pressures as low as $15psi$ this turbulator generated a boundary layer that was turbulent upstream of the ramp.

In the subsequent analysis, the flat plate and ramp are assumed to be adiabatic; however, no measurements are made to verify this assumption.

2.3 Instrumentation and Data Reduction

2.3.1 Wind Tunnel Parameters

The wind tunnel parameters that are measured with the existent instrumentation are the stagnation pressure p_0, the stagnation temperature T_0, and the the test section's static pressure p. It was found in the course of the experiments that the measured static pressure was not consistent with the free-stream Mach number of $Ma = 3.5$ - this measurement was therefore not used. The static pressure is instead determined from a Pitot probe measurement in the free stream (see section 2.3.3) and the assumption that there is a normal shock upstream of the probe tip.

The bleed valves are opened and closed during a wind tunnel run to modify the level of free stream disturbances.

Table 2.1 summarizes the test conditions. The duration of a typical wind tunnel run is one to two hours.

p_0 (psia)	T_0 (K)	$R \cdot 10^{-6}$ (1/m)
15	292	6.2
20	300	7.9
25	300	9.9
35	300	13.8
50	300	19.8
65	300	25.7

Table 2.1: Test conditions

2.3.2 Focusing Schlieren System

As part of this project, a focusing schlieren system was designed and setup in SLDT to visualize the shock/boundary layer interaction. The focusing schlieren technique minimizes the spanwise integration property of conventional schlieren systems [24, 32]. The focusing schlieren image is that of a narrow slice of flow, which is located along the plane of best focus. Thus the focusing schlieren technique is well suited to the investigation of shock

unsteadiness in STBLI, as it is known that the shock motion is not two-dimensional. Indeed, the spanwise "rippling" of the shock foot usually results in a "layered" appearance of the shock when a conventional schlieren system is used [23, 28].

The present focusing schlieren system is based on the design of Weinstein [32]. However, some details are modified to meet both the specific needs of the experiments and the geometric constraints of the wind tunnel. A primary objective of the present design is a small depth of field without use of a large imaging lens. A second objective is to have the capability of taking short duration (that is, microsecond) images of the flowfield. Nevertheless it is not necessary to have a very large field of view for the present experiments. A schematic of the focusing schlieren system is shown in Fig. 2.4. The primary dimensions are: $L = 1397mm$, $l = 635mm$, $L' = 560mm$, and $l' = 1081mm$. The plane of best focus is coplanar with the mid-span section of the compression ramp model.

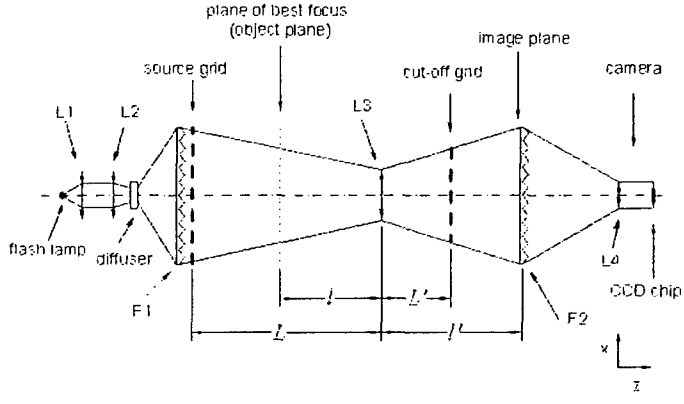

Figure 2.4: Description of focusing schlieren system

The illumination optics of the focusing schlieren consist of a short duration flash lamp (Spectralite 919), two collimating lenses (L1, L2), a diffuser, a Fresnel lens (F1) and a source grid. The two collimating lenses generate a

light spot at the diffuser. The Fresnel lens F1 acts as a light condenser and focuses this light source onto the imaging lens L3. The diffuser is made of two sheets of holographic diffusing material, that have a high transmittance and a spreading angle of $\approx 10 degrees$.

The imaging optics are comprised of the imaging lens L3, a cut-off grid, the Fresnel lens F2 and the camera lens L4. The cut-off grid is a photographic negative image of the source grid; this cut-off grid can be translated in the x direction to vary the schlieren sensitivity. The Fresnel lens F2 is located in the image plane of L3, and it thus determines the plane of best focus in the flow field. This Fresnel lens F2 acts as a relay lens and condenses the light onto the aperture of the camera lens L4, which then transmits the schlieren image onto a CCD chip. The characteristics of the lenses are summarized in Table 2.2.

Lens	Focal Length (mm)	Aperture (mm)
L1	50	50
L2	100	50
L3	400	75
L4	12.5	8.9
F1	150	150
F2	100	200

Table 2.2: Dimensions of lenses in focusing schlieren system

The schlieren image is recorded with a Pulnix TM-1040 video camera, which has a CCD chip of dimensions $9.1mm \times 9.2mm$. The dimensions of the square source grid are $150mm \times 150mm$. On the grid are vertical black stripes, $2mm$ in width, and $1mm$ wide transparent stripes; this grid is made using a photoplotter. The exposure of the cut-off grid is accomplished by replacing the illumination optics with a standard $15W$ light bulb operated on a line voltage of 25 Volts. The grid is exposed for 8 seconds on a $4''$ $\times$ $5''$ Kodak Technical Pan film and then developed for 2 minutes using Kodak D-19 developer at $22°C$. The cut-off grid is exposed *in situ* when the test section of SLDT is empty, but with all the optical components in

place. Particular care is taken to expose and develop the cut-off grid in total darkness.

The performance of the focusing schlieren system can be assessed using the formulae derived by Weinstein [32]. Assuming that the smallest change in brightness that can be detected is 10%, the sensitivity of the focusing schlieren system is given by:

$$\epsilon_{min} = 20626 \frac{aL}{L'(L-l)} arcsec \tag{2.1}$$

where a is the half-height of the dark cut-off gridlines [32]. It should be noted that the 10% criterion was developed for images made on film paper. Modern digital imaging systems actually provide for the detection of much smaller changes in brightness, thus their sensitivity is correspondingly higher.

The resolution of features in the test section is given by:

$$w = \frac{2(l'-L')\lambda}{mb} \tag{2.2}$$

where λ is the wavelength of the light, m is the object magnification, and b is the clear height of the cut-off gridlines.

The major parameter that determines the depth of field is the quantity $R = l/A$, that is the ratio of the distance l from object to imaging lens (L3 in Fig. 2.4) and the imaging lens aperture A. The depth of field of an imaging system depends on the size of an acceptable blur caused by defocusing: if B is the size of the blur, then the depth of field is the product $2RB$ [27]. For a focusing schlieren system, Weinstein [32] defines a depth of unsharp focus DU as the product when a blur of size $2mm$ is used, so that $DU = 4R$ (in mm). R is also related to the number of gridlines that form the image of the schlieren object. If the source grid has n source lines per millimeter, the number of gridlines that blend to form an image, N, is given by:

$$N = \frac{(L-l)n}{R} \tag{2.3}$$

The theoretical field of view F_{th} is given by:

$$F_{th} = A + \frac{l(D-A)}{L} \tag{2.4}$$

where D is the size of the source grid. With $D = 150mm$, this yields a theoretical field of view of 109mm. In the present case, however, the camera lens also limits the field of view. Indeed, the practical field of view F_{pr} is given by the largest portion of the image plane that can be imaged by the camera lens. The camera lens is mounted 110mm behind the image plane (the Fresnel lens F2), so that the magnification factor is 0.13. For a CCD chip that is 9mm square, this gives a maximum image size of 70mm at the image plane, and a corresponding field of view of 41mm in the object plane. This smaller field of view is well suited for the STBLI experiments for which the schlieren system is designed.

Table 2.3 summarizes the characteristics of the present system.

Quantity	Unit	Value
a	mm	0.20
b	mm	0.80
ϵ_{min}	arcsec	13.5
λ	μm	0.5
m	-	1.70
w	mm	0.39
R	-	8.47
DU	mm	34
n	1/mm	0.33
N	-	30
F_{pr}	mm	41

Table 2.3: Characteristics of the focusing schlieren system

A representative schlieren image obtained with the present system is shown in Fig. 2.5. The stagnation pressure is $50psi$ and the cut-off is 50%. The dark region on the left of the image is the edge of the test section window, while the the dark regions along the bottom and the right of the image are shadows of the wind-tunnel model. The concentric rings that are evident in Fig. 2.5 are caused by the grooves in the Fresnel lens F2. Using a regular lens instead of the Fresnel lens would give a smoother picture.

However, no such lens was available at the time of the tests.

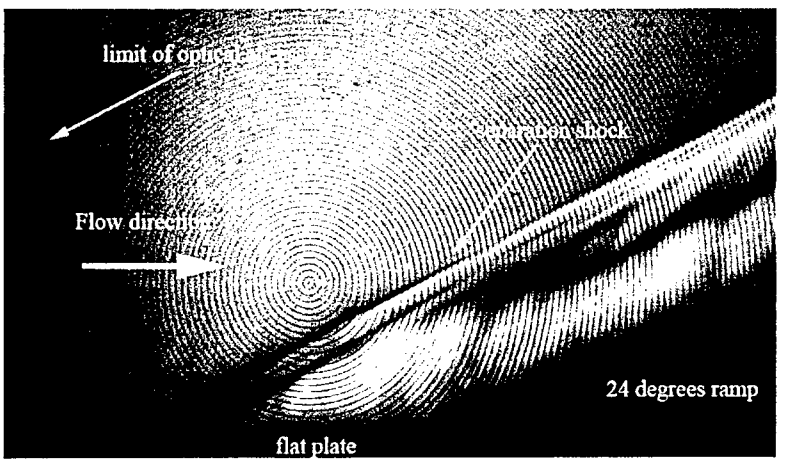

Figure 2.5: Focusing schlieren image of STBLI

The integration time of the Pulnix CCD camera is 1/4000 seconds, which is too large to obtain an instantaneous image in a supersonic flow. Thus instantaneous images are obtained by using the flash lamp as the light source in the darkened wind tunnel room. The flash duration is $1\mu s$, which is small enough to yield an instantaneous image of the flow.

It should be noted that some development work was necessary before obtaining an image similar to that in Fig. 2.5. Initially, a sheet of diffusing material was used as a screen and mounted at the back of the Fresnel lens F2. Although the use of this screen eliminated the rings from the Fresnel lens, the resulting image was too dark for subsequent analysis. A second problem that was encountered during the design of the focusing schlieren system arose from the reflection of light off the model. This reflection arises since the focusing schlieren system uses a light beam, through the test section, whose light rays are at different angles. This is in contrast to a standard schlieren system that uses a light beam with parallel light rays. The light beam in the focusing schlieren system emanates from its extended light source. Thus there may be some reflection of light off the model's surface. For example,

in the present work it is observed that some light rays emanating from the source grid are reflected off the ramp surface before reaching the cut-off grid. These rays are improperly cut-off by the grid and result in a blurry schlieren image. To minimize this problem, one narrow mask is placed on the source grid to limit the angular range of the light rays that reach the model. A second mask is placed on the cut-off grid to block out the light rays that are reflected off the ramp. These masks result in a schlieren image that is of better quality than an image that is made without the masks.

2.3.3 Pitot Pressure Probe

Profiles of the mean quantities in the incoming boundary layer are measured with a Pitot pressure probe. The probe tip is a hypodermic tubing with a wall thickness of $0.005''$ $(0.13mm)$. The probe tip is flattened to an outer height of $0.025''$ $(0.64mm)$ and outer width of $0.040''$ $(1mm)$. The inner height of the probe is $0.015''$ $(0.38mm)$. The probe is connected to a 1000-Torr MKS Barotron pressure transducer (with a $20psi$ range) and the signal is read with a MKS Type 670 signal conditioner. The probe is traversed across the boundary layer using the SLDT traverse system. In the data reduction, no displacement correction, for the tip geometry, is applied.

The free-stream Mach number M_e is determined using the measured Pitot pressure, outside the boundary layer, and the measured tunnel stagnation pressure. The total pressure ratio across a normal shock, upstream of the probe tip, is given by:

$$\frac{p_{t2}}{p_{t1}} = \left[\frac{\gamma+1}{2\gamma M_1^2-(\gamma-1)}\right]^{1/(\gamma-1)} \left[\frac{(\gamma+1)M_1^2}{(\gamma-1)M_1^2+2}\right]^{\gamma/(\gamma-1)} \tag{2.5}$$

where M_1 is the Mach number upstream of the shock and the ratio of specific heats is $\gamma = 1.4$ [21].

The static pressure p is assumed to be constant across the boundary layer and is computed using the isentropic relation:

$$p = p_0 / \left(1 + \frac{\gamma-1}{2} M_e^2\right)^{\gamma/(\gamma-1)} \tag{2.6}$$

where p_0 is the wind-tunnel stagnation pressure reading and M_e is obtained from equation 2.5, since $M_e = M_1$.

The Mach number profile $M(y)$ across the boundary layer is computed using the Pitot-Rayleigh relation:

$$\frac{p_t}{p} = \left[\frac{\gamma+1}{2}M^2\right]^{\gamma/(\gamma-1)} \left[\frac{(\gamma+1)}{2\gamma M^2-(\gamma-1)}\right]^{1/(\gamma-1)} \tag{2.7}$$

where p_t is the measured Pitot pressure and p is the static pressure.

The static temperature profile $T(y)$ is computed using the isentropic relation:

$$T = T_0/\left(1+\frac{\gamma-1}{2}M^2\right) \tag{2.8}$$

where T_0 is assumed constant across the boundary layer and the value of the measured wind-tunnel stagnation temperature is used.

The velocity profile $u(y)$ and density profile $\rho(y)$ are respectively calculated using the definition of the Mach number and the ideal gas law:

$$u = M\sqrt{\gamma RT} \tag{2.9}$$

$$\rho = \frac{p}{RT} \tag{2.10}$$

where the perfect gas constant is $R = 287 J/kgK$.

The velocity profiles in wall units ($u^+ = f(y^+)$) are obtained using the Van Driest II compressibility correction [28], and the value of the friction factor c_f is determined using a Clauser chart method.

2.3.4 Hot-Wire Probe

The mass flow fluctuations are measured in the tunnel free-stream and in the boundary layer upstream of the ramp using a hot-wire probe. The probe is a Dantec 55P11 miniature hot-wire probe, whose prongs are stiffened with epoxy. A wire of $5\mu m$ diameter and approx. $1mm$ in length is spot welded to the prong's tip. The wire is mounted with some slack to avoid strain-gaging effects.

The hot-wire probe is operated with a Dantec Streamline Constant Temperature Anemometer that is equipped with a 1:1 bridge. The frequency response, determined using the internal square wave test, is $20kHz$. This relatively low frequency response is thought to arise from the mismatch of impedances in the active and passive arms of the bridge. Thus the transfer function of the CTA is measured *in situ* and the procedure, detailed in Weiss *et al* [33], is used to correct the fluctuation measurements up to a frequency of $100kHz$.

The output voltage of the CTA is separated into AC and DC parts that are then recorded with an HP1429 digital acquisition card. The AC part is high-pass filtered at $10Hz$ and low-pass filtered at $500kHz$. The DC record is unfiltered. Blocks of 2^{25}, that is 524288, samples are acquired at a sampling rate of $1MHz$.

The hot-wire is calibrated in the free-stream of the wind tunnel. The stagnation pressure is varied from $20psi$ to $65psi$. To allow the extrapolation of the calibration data to lower stagnation pressures, a King's law type of calibration curve is used:

$$E^2 = A + B(\rho u)^n \tag{2.11}$$

where A, B, and n are determined from a least-squares-error fit the experimental data. Typical calibration data is shown in Fig. 2.6

The overheat ratio of the hot-wire is $a_w = (R_w - R_a)/R_a$, where R_a is the wire resistance at ambient temperature. For the present work $a_w = 0.8$; therefore, it is assumed that the wire is only sensitive to mass flow fluctuations [29]. The normalized fluctuating wire voltage is therefore be written as:

$$\frac{e_{rms}}{\overline{e}} = S_{\rho u}\frac{(\rho u)_{rms}}{\overline{\rho u}} \tag{2.12}$$

where the normalized sensitivity to mass flow fluctuations is given by Smits *et al* [29]:

$$S_{\rho u} = \frac{nB\overline{\rho u}^n}{2(A + B\overline{\rho u}^n)} \tag{2.13}$$

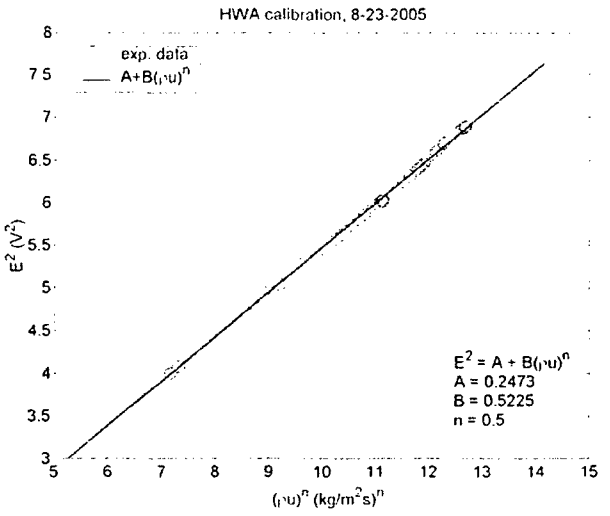

Figure 2.6: Representative hot-wire calibration

Thus, measurement of e_{rms} enables the computation of $(\rho u)_{rms}$ using the previously determined calibration coefficients A, B, and n.

In the empty test section of the wind tunnel, the mass flow fluctuations are caused by the pressure fluctuations radiated from the turbulent boundary layer on the nozzle walls [4, 20]. Assuming that the noise sources are stationary, the pressure fluctuations are given by Laufer [20] as:

$$\frac{p_{rms}}{\overline{p}} = \frac{\gamma M^2}{M^2 - 1} \frac{(\rho u)_{rms}}{\overline{\rho u}} \tag{2.14}$$

2.3.5 Hot-Film Probe

The unsteadiness of the separation shock is measured with a cylindrical Dantec 55R01 hot-film probe. The probe is comprised of a $70\mu m$ diameter cylindrical quartz fiber that is $3mm$ in length and covered by a $0.1\mu m$ thick nickel film. The probe is positioned at a height of $y = 1.5\delta$ above the flat plate and traversed parallel to the plate across the separation shock. Since

hot-wires repeatedly broke in the harsh environment of the fluctuating shock, a cylindrical hot-film probe is used.

The probe is operated with the Dantec Streamline CTA equipped with the 1:1 bridge. The CTA's frequency response is $\approx 20kHz$, which is sufficient to investigate the variations of mass flow that are caused by the motion of the separation shock. The output voltage is low-pass filtered at $200kHz$ and blocks of 2^{25} samples are acquired at a sampling rate of $400kHz$ using the HP1429 digital acquisition card.

The hot-film probe is calibrated in the tunnel's free-stream using a method similar to that used for the hot-wire. A time trace of the mass flow fluctuations is then be derived from the measured output voltage. Three typical time traces measured upstream, at the mean position, and downstream of the separation shock, respectively, are shown in Fig. 2.7. When the sensor is upstream of the shock, the mass flow is at the free-stream value of $55kg/m^2s$. Downstream of the shock, the mass flow increases to $105kg/m^2s$ due to the compression by the shock. When the sensor is located at the mean shock position, the signal is intermittent and the mass flow fluctuates between the free-stream and downstream values - these fluctuations are indicative of the oscillations of the separation shock across the sensor.

The streamwise extent of the shock's oscillation, L_i, (the "intermittent length") is measured by plotting the RMS of the fluctuating mass flow relative to the sensor position. The RMS rises due to the intermittent motion of the shock, thus the width of the RMS peak is a measure of the length scale of the shock oscillation. This length scale can also be inferred from the intermittency distribution γ, where γ is defined as the fraction of the time that the shock is upstream of the sensor. Thus $\gamma = 0$ when the shock is always downstream of the sensor; conversely $\gamma = 1$ when the shock is always upstream of the sensor. For a given time trace, the position of the shock is determined by comparing the instantaneous mass flow to a specified threshold. When $\rho u(t)$ is larger than the threshold value, the shock is determined to be upstream of the sensor; conversely, when $\rho u(t)$ is smaller than the threshold value, the shock is determined to be downstream of the sensor. In the present work, the threshold is set as the average of the upstream and

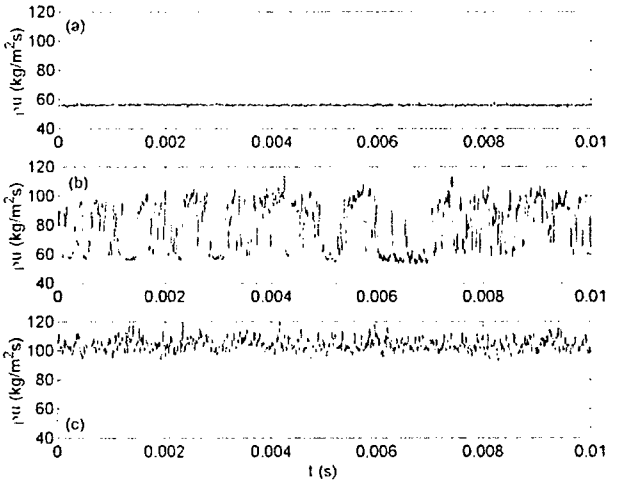

Figure 2.7: Time traces of fluctuating mass flow measured with the hot-film sensor ($p_0 = 20psi$): (a) sensor located upstream of shock; (b) sensor located at mean shock location; and (c) sensor located downstream of shock.

downstream mass flow values. Figure 2.8 illustrates the two methods of the determining the intermittent length, L_i. In the subsequent discussion, the intermittent length L_i is defined as the distance between the last station where γ is exactly 0 and the first station were γ is exactly 1.

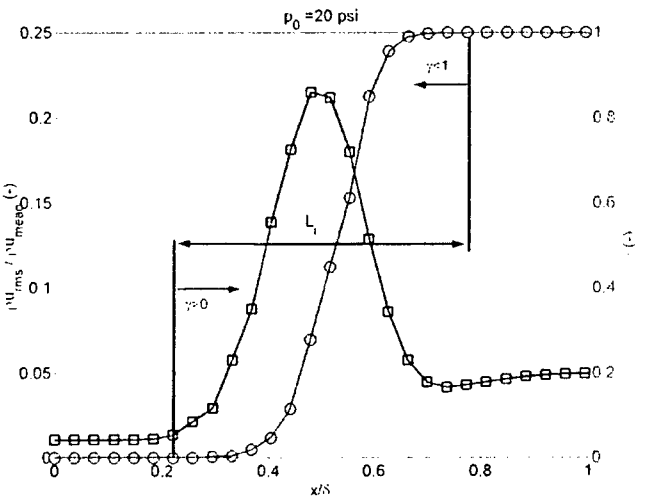

Figure 2.8: Definition of the intermittent length, L_i

Chapter 3

Results and Discussion

3.1 Flow Quality in SLDT

The free-stream disturbance levels in the test section of SLDT are measured using the hot-wire anemometry described in section 2.3.4. These results are discussed here and the related figures are presented in Appendix A.

The level of static pressure fluctuations corresponding to the flow conditions (see Table 2.1) are shown in Figs. A.1 to A.6. The curves labeled bvc and bvo, respectively, refer to tunnel operation with bleed valves closed and bleed valves open, respectively. The station $x = 0$ corresponds to the ramp corner and negative x values correspond to stations that are upstream of the ramp corner. The leading edge of the flat plate is located at $x_{LE} = -10inch$.

For stagnation pressures less than $65psi$, the fluctuation levels increase in the downstream direction when the bleed valves are open. On the otherhand when the bleed valves are closed, the levels are either constant, for $p_0 = 15psi$, or decrease slightly, for $p_0 \geq 15psi$ and $< 65psi$. The increase in fluctuation levels, for the bleed valves open case, is a consequence of the laminar/turbulent transition of the nozzle wall boundary layers. When the nozzle boundary layer is laminar, the fluctuation levels are very low ($\approx 0.1\%$) and close to instrument electronic noise level. When the nozzle boundary layer is turbulent, the fluctuation levels are higher ($\approx 0.5\%$, depending on the Reynolds number). The radiation of acoustic waves from

the supersonic turbulent boundary layers produces these higher levels [20]. For the bleed valves closed case, the fluctuation levels are always relatively high, but the levels decrease, slightly, both with increasing x and increasing Reynolds number. This decrease is a consequence of the attendant change in the boundary layer thickness and its' related acoustic radiation properties [2]. At a stagnation pressure of $65psi$, the variations in the disturbance levels are similar for both the bvc and bvo cases. The fluctuation levels increase with increasing x and are a maximum at 4-6 inches upstream of the ramp's corner.

The spectral distributions of free-stream disturbances are presented in Figs. A.7 to A.18 for both bvc and bvo cases. For the bvc case, the spectra have a maximum at $10 - 20kHz$, depending on the Reynolds number. For stagnation pressures lower than $25psi$, there are also marked peaks at around $4 - 5kHz$. The source of these peaks, which are not seen above $25psi$, is unknown. When the bleed valves are open, the shape of the spectra is quite different: for the more upstream positions, the PSDs are flat and close to instrument noise level.[1] At the more downstream positions, there is a broadband rise in the spectral levels with increasing x. For the $p_0 = 65psi$ case, the PSD distributions are similar for both the bvc and bvo cases. This is the case, since the nozzle boundary layers are turbulent in both cases.

For all streamwise positions, at stagnation pressures less than $25psi$, the quantitative details of the spectra depend upon the bleed valves position. Thus, the turbulent boundary layer on the model develops in a "quiet" environment when the bleed valves are open and develops in a "noisy" environment when the bleed valves are closed. For the bvo cases of $p_0 = 15psi$ and $20psi$, the quiet flow extends up to the compression ramp corner.

[1] The usual f^2 rise due to electronic noise is not seen in the spectra as the signals for the lowest freestream noise levels are close to instrument noise level (Note that, the signals are not preamplified), and the PSDs are not corrected for the anemometer's transfer function.

3.2 Characteristics of Incoming Boundary Layer

The characteristics of the incoming boundary layer are detailed from measurements at $x = -0.53''$ ($x = -13.5mm$), which is upstream of the ramp corner. This position is, depending on the stagnation pressure, (2-4)δ upstream of the corner. The measurements are made in the absence of theremovable ramp. The mean flow properties are measured with the Pitot probe and the fluctuating properties with the hot-wire. For the measurements at $p_0 = 15, 20, 25$, and $35psi$ the flat plate is equipped with *Turbulator 2*. For the measurements at $p_0 = 50$ and $65psi$, the plate is equipped with *Turbulator 1* (see section 2.2 for details).

3.2.1 Mean-Flow Properties

The mean-flow properties of the incoming boundary layer are derived from the Pitot pressure measurements described in section 2.3.3. A constant static pressure and total temperature across the boundary layer are assumed. The plots of the Pitot pressure and velocity profiles are presented in Appendix B. The mean-flow properties of the incoming boundary layer are summarized in Table 3.1 for BVO operation and in Table 3.2 for BVC operation. In Tables 3.1 and 3.2, $H = \delta_1/\theta$ is the usual form parameter and

$$H_i = \frac{\int_0^\delta (1 - u/u_e)dy}{\int_0^\delta (u/u_e)(1 - u/u_e)dy} \tag{3.1}$$

is the corresponding incompressible form factor [8].

At stagnation pressures of $35psi$ and lower, the measured boundary layer thicknesses are similar for the BVO and BVC conditions. This indicates that the transition location is independent of the free-stream disturbance levels. Hence, the *Turbulator 2* is effective in fixing the location of the laminar-turbulent transition. At $50psi$ and $65psi$, however, the boundary layer thicknesses are smaller when the tunnel was operated in the low-disturbance mode (BVO). This is so, since the transition location is more downstream in BVO mode. Hence, *Turbulator 1* does not fix the location of laminar-turbulent transition for both bleed valve cases.

p_0 (psia)	15	20	25	35	50	65
Ma_e (-)	3.48	3.47	3.47	3.47	3.45	3.45
$\delta_{0.99}$ (mm)	6.80	6.90	6.80	6.65	3.80	3.80
θ (mm)	0.340	0.369	0.360	0.348	0.219	0.207
δ_1 (mm)	2.42	2.59	2.55	2.51	1.51	1.53
$Re_\delta \cdot 10^{-4}$ (-)	4.34	5.63	6.92	9.26	7.69	9.99
$Re_\theta \cdot 10^{-3}$ (-)	2.17	3.01	3.66	4.85	4.44	5.45
H (-)	7.1	7.0	7.1	7.2	6.9	7.4
H_i (-)	1.7	1.6	1.6	1.7	1.9	2.0
$c_f \cdot 10^3$ (-)	2.35	2.05	1.90	1.76	1.84	1.72

Table 3.1: Mean-flow properties of boundary layer, BVO

Except for $p_0 = 15psi$, the boundary layer profiles are very similar for both BVC and BVO cases. The velocity profiles with inner-scaling, presented in Appendix B, show that there is a logarithmic region for all cases. At the higher stagnation pressures (that is Reynolds numbers) there is a deviation from the log-law close to the wall; this is a result of the low spatial resolution of the Pitot probe. The friction coefficients c_f obtained by the Clauser method are compared to the Kármán-Shoenherr correlation in Fig. 3.1. The compressible data (c_f, Re_θ) are transformed to the incompressible form ($\overline{c_f}$, $\overline{Re_\theta}$) using the Van Driest II transformation [17]. It is evident, Fig. 3.1, that the data are slightly higher than the correlation. This is thought to be a Reynolds number effect, as the present data are at the lower end of the correlation range. The mismatch may also be due either to the assumption of constant total temperature across the boundary layer or the assumption of an adiabatic wall, as both assumptions are approximation. Nevertheless, the presence of the logarithmic region and c_f that are consistent with the incompressible data suggest that the boundary layer is close to an equilibrium turbulent boundary layer. Except for $p_0 = 15psi$, the mean properties of the boundary layer are independent of the free-stream disturbance levels.

An examination the BVO and BVC velocity profiles, for $p_0 = 15psi$, shows that there are differences at the edge of the boundary layer. In par-

p_0 (psia)	15	20	25	35	50	65
Ma_e (-)	3.45	3.46	3.47	3.49	3.46	3.46
$\delta_{0.99}$ (mm)	6.80	6.90	6.85	6.70	4.10	4.00
θ (mm)	0.362	0.369	0.364	0.351	0.234	0.222
δ_1 (mm)	2.56	2.73	2.65	2.61	1.67	1.61
$Re_\delta \cdot 10^{-4}$ (-)	4.49	5.63	6.97	9.33	8.30	10.51
$Re_\theta \cdot 10^{-3}$ (-)	2.39	3.01	3.71	4.89	4.75	5.83
H (-)	7.1	7.4	7.3	7.4	7.1	7.3
H_i (-)	1.7	1.6	1.6	1.7	1.9	1.9
$c_f \cdot 10^3$ (-)	2.15	2.05	1.90	1.76	1.84	1.72

Table 3.2: Mean-flow properties of boundary layer, BVC

ticular, the Pitot pressures are marked different at $y \simeq 6mm$. Although the reason for this difference is unclear, it is thought to be the result of a Mach wave that originates from the nozzle or sidewalls. Indeed, it is known that laminar-turbulent transition on the nozzle or sidewall boundary-layer can result in Mach number non-uniformities in the test section of SLDT at low stagnation pressures. If an oblique Mach wave intersects with the boundary layer on the model, the assumption of a constant static pressure is then invalid and the velocity profiles derived from the measured Pitot pressures are then erroneous. This may be the source of the difference in BVO and BVC velocity profiles at $p_0 = 15psi$ shown in Figs. B.2 and B.3.

3.2.2 Fluctuating Properties

The fluctuating mass flow profiles in the incoming boundary layer are measured with the hot-wire technique described in section 2.3.4. It is assumed that the probe is sensitive only to the longitudinal mass flow ρu. Smits *et al* [29] show that this assumption is valid provided that the wire overheat is high and the Mach number is greater than 1.5. In the present work, $a_w = 0.8$. Figure 3.2 shows the Mach number profile in the incoming boundary layer at $p_0 = 20psi$; this is typical of all cases. It is seen that the Mach number is greater than 1.5 at all measurement stations.

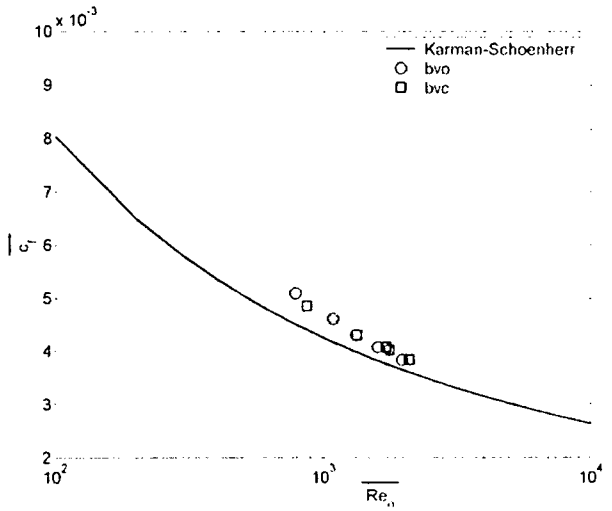

Figure 3.1: Incompressible skin friction coefficient, data transformed using Van Driest II transformation

The profiles of the fluctuating mass flow are presented in Appendix C. For stagnation pressures of $p_0 \geq 20psi$, the profiles are similar for both BVO and BVC cases. These results confirm that the free-stream disturbance levels do not affect the state of the incoming boundary layer. The maximum level of mass flow fluctuations is approximately 15% and at $y/\delta \simeq 0.5$. This is in good agreement with previously measured data [29]. The large level of fluctuations very close to the wall is thought to be due to wall interference effects. An examination of the spectra reveals that the mass flow fluctuations are broadband in character; the spectral levels do not decrease significantly below the anemometer's cut-off ($100kHz$). Thus, it is thought that the actual mass flow fluctuations in the boundary layer are larger than these measured values.

At $p_0 = 15psi$, there is a significant difference in the profiles for BVC and BVO operation. The mass flow fluctuations for the BVC case are similar to those obtained at higher stagnation pressures, whereas for the BVO case

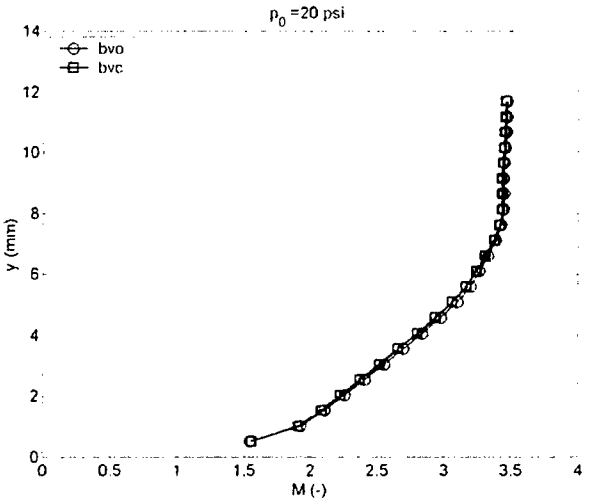

Figure 3.2: Mach number profile in the incoming boundary layer, $p_0 = 20psi$

the fluctuations are larger. Furthermore in the spectra, there are significant peaks at $f \approx 10kHz$ and corresponding harmonics; these peaks are more pronounced for BVO case than the BVC case. The source of these peaks is unknown but the peaks are possibly related to the presence of an moving Mach wave that originates from the nozzle boundary layer, as discussed in section 3.2.1.

3.2.3 Summary of Incoming Boundary Layer Properties

In summary, the state of the incoming boundary layer can be classified as follows with respect to the stagnation pressure:

- For $p_0 = 20$, 25, and $35psi$, the boundary layer is identical for the BVC and BVO cases. Transition at the leading edge of the flat plate is successfully accomplished using the *Turbulator 2*, and the resulting boundary layer thicknesses are independent of the free-stream disturbance levels. The mean and fluctuating properties of the boundary

layer are also independent of the free-stream disturbance levels.

- For $p_0 = 50$ and $65psi$, there are differences in boundary layer thicknesses. When the tunnel is operated in the quiet mode (that is BVO), boundary layer transition occurs downstream of the leading edge. That is, the *Turbulator 1* that is used is only effective under BVC condition. However, the boundary layer's mean and fluctuating properties are seen to be independent of the free-stream disturbance levels.

- For $p_0 = 15psi$, the boundary layer characteristics are different between the BVC and BVO cases. The mass flow fluctuations for the BVC case are similar to those at $p_0 = 20$, 25, and $35psi$, whereas for the BVO case the fluctuations are larger. The cause of the discrepancy is thought to arise from a Mach wave that is generated on the nozzle or sidewalls.

3.3 Schlieren Images of the STBLI

Representative focusing schlieren images are presented in Appendix D. (Note that as no image was available for $p_0 = 65psi$ a focusing schlieren image for $p_0 = 75psi$, which is quite similar, is presented.) The cut-off is 50% for all images and the microsecond duration spark light source is used.

The sensitivity of the focusing schlieren system is not sufficient to capture the turbulent structures in the boundary layer, however the strong compression due to the shock wave is identifiable. The shock foot is located upstream of the compression ramp: this is an indication that the boundary layer is separated, as data from the literature suggest that there is a large separation zone for a ramp angle of 24^o. At the higher stagnation pressures, the compression is strong and the separation shock penetrates well into the boundary layer. The depth of penetration is smaller at lower pressures.

The separation shock is not very sharp in the images. Instead of a sharp line, the separation shock appears as a broad, dark region. This is attributed to the spanwise "rippling" of the separation region, which is also observed in conventional schlieren images [28]. Thus the focusing capabilities of the

present focusing schlieren system are not sufficient to provide a more crisp visualization of the separation shock.

Nevertheless some conclusive observation can be made from the schlieren images. In the range $p_0 = 15 - 35psi$, the flow structure is similar for both the BVC and BVO cases. Thus, the free stream disturbance levels do not have an effect on the shock location nor its strength. At $p_0 = 50$ and $75psi$, the shock is located slightly more downstream when the bleed valves are open. This is due to the difference in boundary layer thickness between BVC and BVO cases, as it is known that the interaction length roughly scales with the incoming boundary layer thickness when other parameters are held constant [8, 25]. It is interesting to note that the position of the separation shock (which is a measure of the upstream interaction length) is more-or-less constant over the range of stagnation pressures examined, even though the incoming boundary layer thickness is smaller between the BVC and BVO cases (see Tables 3.1 and 3.2 for $p_0 = 50psi$ and $65psi$ conditions).

3.4 Characteristics of Unsteady Shock Motion

The unsteady behavior of the separation shock is investigated using a cylindrical hot-film, as described in section 2.3.5. The sensor is positioned at $y = 1.5\delta$ and traversed streamwise across the separation shock. The shock motion across the sensor produces an intermittent signal, the plots of which are presented in Appendix E. In these plots, along the x-axis, x, is normalized by the incoming boundary layer thickness, δ; along the y-axis, the mass flow RMS is normalized by the mean mass flow upstream of the shock. The intermittent length, L_i, is derived from these measurements using the intermittency, γ, as described in section 2.3.5.

For $p_0 = 20$, 25, and $35psi$ the unsteady behavior of the separation shock is similar for both BVC and BVO cases. Both the mean shock position and the streamwise extent of the intermittent region are the same for the BVC and BVO cases. Thus, the free-stream disturbance level does not influence the unsteady behavior of the separation shock. This observation is consistent with the schlieren images, which also show that there are no significant

differences between the two cases.

For $p_0 = 50$ and $65psi$, the mean shock position is further downstream for the BVO case compared to BVC case. This is in good agreement with the schlieren images shown for $p_0 = 50$ and $75psi$. The difference in the position of the separation shock is due to the difference in the boundary layer thickness δ, which is smaller for the BVO case. On the other hand, the streamwise extent of the intermittent region is similar for both BVC and BVO cases. Thus, the free-stream disturbance levels do not affect the unsteady behavior of the separation shock.

For $p_0 = 15psi$, the mean shock position is also located more downstream when the bleed valves are open. In this case, however, the incoming boundary layer thicknesses are similar for both BVC and BVO cases. Nevertheless, the results of section 3.2 indicate that there is a difference in the state of the boundary layer at this stagnation pressure. This may explain the difference in the mean shock position, although the physical causes for this difference are unknown. At this pressure, the streamwise extent of the intermittent region is similar for BVO and BVC operation.

The measured intermittent lengths are summarized in Table 3.3. L_i varies little between $3.6mm$ and $4.3mm$. On the other hand, there is a relatively large variation in the boundary layer thickness over the same range of stagnation pressures. Thus, the normalized intermittent length, L_i/δ, is in the range 0.5 to 1.0.

	BVC		BVO	
p_0 (psi)	L_i (mm)	L_i/δ (-)	L_i (mm)	L_i/δ (-)
15	3.6	0.52	3.8	0.56
20	3.8	0.55	3.8	0.55
25	4.1	0.60	4.3	0.64
35	4.1	0.61	4.3	0.64
50	3.8	0.93	3.6	0.94
65	4.1	1.02	3.8	1.00

Table 3.3: Intermittent length L_i, defined as the region where $0 < \gamma < 1$ (see 2.3.5)

Representative spectra at a stagnation pressure of $p_0 = 20psi$ with the bleed valves closed, measured upstream, at the mean location, and downstream of the separation shock are shown in Fig. 3.3. Upstream of the shock, the fluctuations are low, since only the acoustic radiation from the turbulent boundary layer is measured. Downstream of the shock, the measured fluctuations are larger. At the mean shock location, the fluctuations are substantially larger and the spectral levels at low frequencies are the largest. The passage of the shock across the sensor produces these elevated levels. It is evident that time scale of the shock motion is longer than the typical time scales in the boundary layer [10, 15].

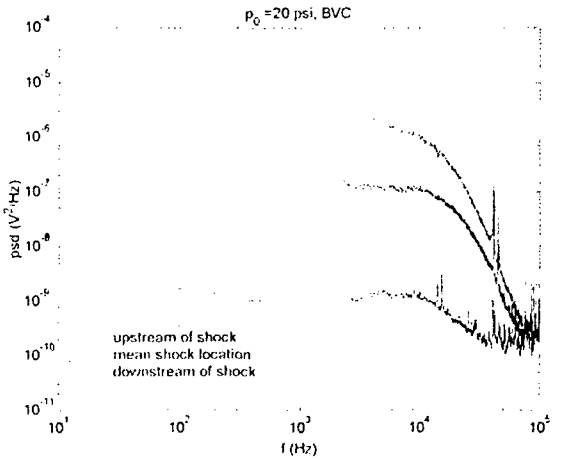

Figure 3.3: Spectra of mass flow fluctuations in the intermittent region, $p_0 = 20psi$

Chapter 4

Concluding Remarks

The effect of free-stream noise on the flow structure of a supersonic compression ramp is investigated in the Mach 3.5 Supersonic Low Disturbance Tunnel (SLDT) at the NASA Langley Research Center. The free-stream disturbance levels are varied by opening or closing the nozzle bleed valves. With bleed valves open (BVO) the tunnel is in a "quiet" mode and the level of free-stream disturbances is very low. With bleed valves closed (BVC), the level of free-stream disturbances is comparable to that in a conventional wind tunnel. A separated shockwave/turbulent boundary layer interaction is generated on a 24^o compression ramp mounted on a flat plate model. The boundary layer is fully turbulent and the Reynolds number based on momentum thickness is the range $Re_\theta = 2170 - 5830$. The structure of the interaction is visualized using a focusing schlieren system and the unsteady behavior of the separation shock is measured with a hot-film probe.

The present results show that the separation shock is characterized by large-scale, low-frequency, oscillations that are comparable to those observed in previous experiments performed in conventional facilities at higher Reynolds numbers. The intermittent length of the interaction is in the range $L_i/\delta \simeq 0.5 - 1.0$. This result is comparable to observations in previous compression ramp experiments [11, 14]. However, these values of L_i are larger than those obtained in numerical simulations [1, 22, 34].

Although the upstream interaction length L_{ui} is not measured in the the

present experiments, the qualitative schlieren images show that the global interaction length is more-or-less constant. Since the numerical value of L_i is also more-or-less constant, this suggests that L_i scales with L_{ui} and not with the boundary layer thickness. This observation is in agreement with the recent results of Dupont *et al* [15], that are obtained for an impinging shock/turbulent boundary layer interaction.

The high level of free-stream noise can have an indirect effect on the interaction by triggering laminar-turbulent transition earlier in "noisy" compared to "quiet" conditions. The earlier transition modifies the incoming boundary layer thickness and thus the global scale of the interaction. On the other hand, the unsteady behavior of the separation shock is independent of the free-stream disturbance levels. Thus, wind tunnel free-stream noise does not appear to be the source of the discrepancies, between experiment and simulation, that have been previously observed.

Bibliography

[1] N. A. Adams. Direct Simulation of the Turbulent Boundary Layer Along a Compression Ramp at $M = 3$ and $Re_\theta = 1685$. *Journal of Fluid Mechanics*, 420:47–83, 2000.

[2] J. B. Anders, P. C. Stainback, and I. E. Beckwith. New Technique for Reducing Test Section Noise in Supersonic Wind Tunnels. *AIAA Journal*, 18(1):5–6, 1980.

[3] J. Andreopoulos and K. C. Muck. Some New Aspects of the Shock-Wave/Boundary Layer Interaction in Compression Ramp Flows. *Journal of Fluid Mechanics*, 180:405–428, 1987.

[4] I. E. Beckwith, F.-J. Chen, and M. R. Malik. Design and Fabrication Requirements for Low-Noise Supersonic/Hypersonic Wind Tunnels. AIAA 88-0143, 1988.

[5] S. J. Beresh, N. T. Clemens, and D. S. Dolling. Relationship Between Upstream Turbulent Boundary-Layer Velocity Fluctuations and Separation Shock Unsteadiness. *AIAA Journal*, 40(12):2412–2422, 2002.

[6] NASA Langley Research Center. Wind-Tunnel Model Systems Criteria. NASA LAPG 1710.15, 2003.

[7] F.-J. Chen, M. R. Malik, and I. E. Beckwith. Comparison of Boundary Layer Transition on a Cone and Flat Plate at Mach 3.5. AIAA 88-0411, 1988.

[8] J. M. Délery. Shock Wave/Turbulent Boundary Layer Interaction and its Control. *Progress in Aerospace Sciences*, 22:209–280, 1985.

[9] D. S. Dolling. High-Speed Turbulent Separated Flows: Consistency of Mathematical Models and Flow Physics. *AIAA Journal*, 36(5):725–732, 1998.

[10] D. S. Dolling. Fifty Years of Shock-Wave/Boundary-Layer Interaction Research: What Next? *AIAA Journal*, 39(8):1517–1531, 2001.

[11] D. S. Dolling. Unsteadiness of Shock-Induced Turbulent Separated Flows - Some Key Questions. AIAA 2001-2708, 2001.

[12] D. S. Dolling and L. Brusniak. Separation Shock Motion in Fin, Cylinder, and Compression Ramp-Induced Turbulent Interactions. *AIAA Journal*, 27(6):734–742, 1987.

[13] D. S. Dolling and M. T. Murphy. Unsteadiness of the Separation Shock Wave Structure in a Supersonic Compression Ramp Flowfield. *AIAA Journal*, 21(12):1628–2634, 1983.

[14] D. S. Dolling and C. T. Orr. Unsteadiness of the Shock Wave Structure in Attached and Separated Compression Ramp Flows. *Experiments in Fluids*, 3:24–32, 1985.

[15] P. Dupont, C. Haddad, J. P. Ardissone, and J. F. Debiève. Space and Time Organisation of a Shock Wave/Turbulent Boundary Layer Interaction. *Aerospace Science and Technology*, 9:561–572, 2005.

[16] M. E. Erengil and D. S. Dolling. Correlation of Separation Shock Motion with Pressure Fluctuations in the Incoming Boundary Layer. *AIAA Journal*, 29(11):1868–1877, 1991.

[17] E. J. Hopkins and M. Inouye. An Evaluation of Theories for Predicting Turbulent Skin Friction and Heat Transfer on Flat Plates at Supersonic and Hypersonic Mach Numbers. *AIAA Journal*, 9(6):993–1003, 1971.

[18] Y. X. Hou, Ö. H. Ünalmis, P. C. Bueno, N. T. Clemens, and D. S. Dolling. Effects of Boundary-Layer Velocity Fluctuations on Unsteadiness of Blunt-Fin Interactions. *AIAA Journal*, 42(12):2615–2619, 2004.

[19] D. Knight, H. Yan, A. G. Panaras, and A. Zheltovodov. Advances in CFD Predictions of Shock Wave Turbulent Boundary Layer Interactions. *Progress in Aerospace Sciences*, 39:121–184, 2003.

[20] J. Laufer. Aerodynamic Noise in Supersonic Wind Tunnels. *Journal of the Aeronautical Sciences*, 28:685–692, 1961.

[21] A. Pope and K. L. Goin. *High-Speed Wind Tunnel Testing.* Wiley, 1965.

[22] D. P. Rizzetta and M. R. Visbal. Large-Eddy Simulation of Supersonic Compression-Ramp Flows. AIAA 2001-2858, 2001.

[23] M. S. Selig, J. Andreopoulos, K. C. Muck, J. P. Dussauge, and A. J. Smits. Turbulence Structure in a Shockwave/Turbulent Boundary Layer Interaction. *AIAA Journal*, 27(7):862–869, 1989.

[24] G. S. Settles. *Schlieren and Shadowgraph Techniques.* Springer, 2001.

[25] G. S. Settles, J. J. Perkins, and S. M. Bogdonoff. Upstream Influence Scaling of 2D and 3D Shock/Turbulent Boundary Layer Interactions at Compression Corners. AIAA 81-0334, 1981.

[26] K. Sinha, K. Mahesh, and G. V. Candler. Modeling the Effect of Shock Unsteadiness in Shock/Turbulent Boundary-Layer Interactions. *AIAA Journal*, 43(3):586–594, 2005.

[27] W. J. Smith. *Modern Optical Engineering.* McGraw-Hill, 2000.

[28] A. J. Smits and J. P. Dussauge. *Turbulent Shear Layers in Supersonic Flow.* AIP Press, 1996.

[29] A. J. Smits, K. Hayakawa, and K. C. Muck. Constant Temperature Hot-Wire Anemometer Practice in Supersonic Flows. *Experiments in Fluids*, 1:83–92, 1983.

[30] F. O. Thomas, C. M. Putnam, and H. C. Chu. On the Mechanism of Unsteady Shock Oscillation in Shock Wave/Turbulent Boundary Layer Interactions. *Experiments in Fluids*, 18:69–81, 1994.

[31] Ö. H. Ünalmis and D. S. Dolling. Experimental Study of Causes of Unsteadiness of Shock-Induced Turbulent Separation. *AIAA Journal*, 36(3):371–378, 1998.

[32] L. M. Weinstein. Large-Field, High-Brightness Focusing Schlieren System. *AIAA Journal*, 31(7):1250–1255, 1993.

[33] J. Weiss, H. Knauss, and S. Wagner. Method for the Determination of Frequency Response and Signal to Noise Ratio for Constant-Temperature Hot-Wire Anemometers. *Review of Scientific Instruments*, 72(3):1904–1909, 2001.

[34] M. Wu and M. P. Martin. Direct Numerical Simulation of Shock-wave/Turbulent Boundary Layer Interaction. AIAA 2004-2145, 2004.

Appendix A

SLDT Flow Quality Measurements

The measured static pressure fluctuations along the centerline of the empty SLDT test section and the power spectral density (PSD) of the fluctuations are presented in this appendix. The hot-wire measurement technique is described in section 2.3.4. The location $x = 0$ corresponds to the ramp corner and negative x values correspond to stations upstream of the corner. The leading edge of the flat plate is located at $x_{LE} = -10inch$. The lines labeled "bvc" and "bvo" respectively, refer to the bleed valves closed and open cases respectively. The PSDs are computed from the anemometer output voltages and are in units of V^2/Hz. The PSDs are calculated from blocks of 8192 data samples using Welch's averaged modified periodogram method as implemented in MATLAB. The frequency resolution is $122Hz$.

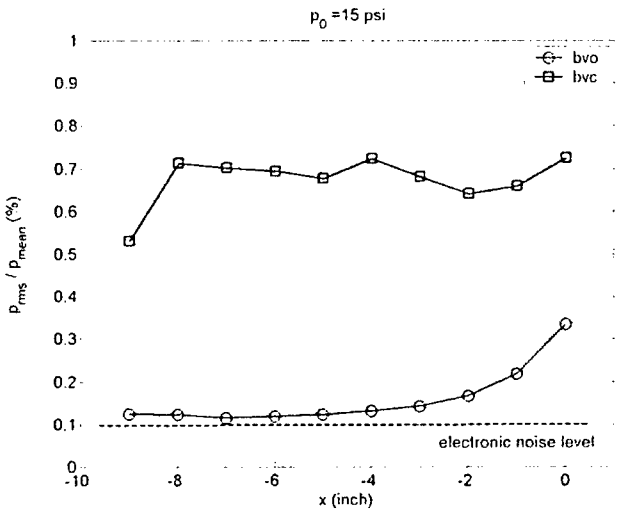

Figure A.1: Static pressure fluctuations along centerline, $p_0 = 15psi$

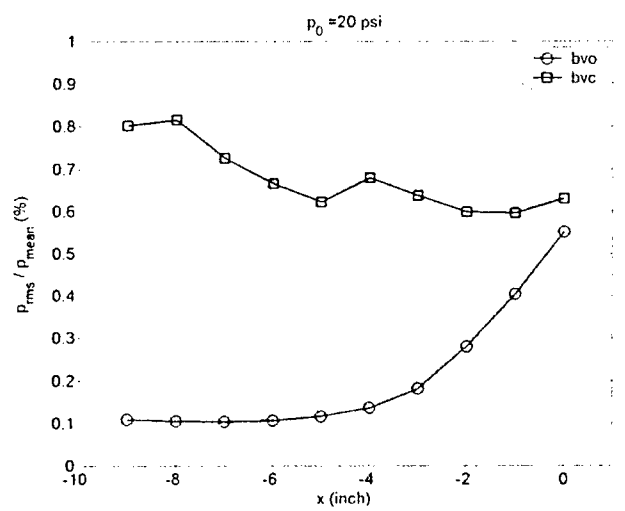

Figure A.2: Static pressure fluctuations along centerline, $p_0 = 20psi$

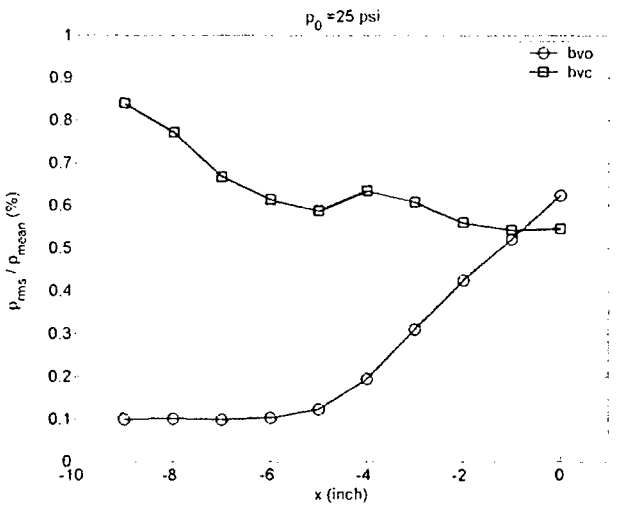

Figure A.3: Static pressure fluctuations along centerline, $p_0 = 25psi$

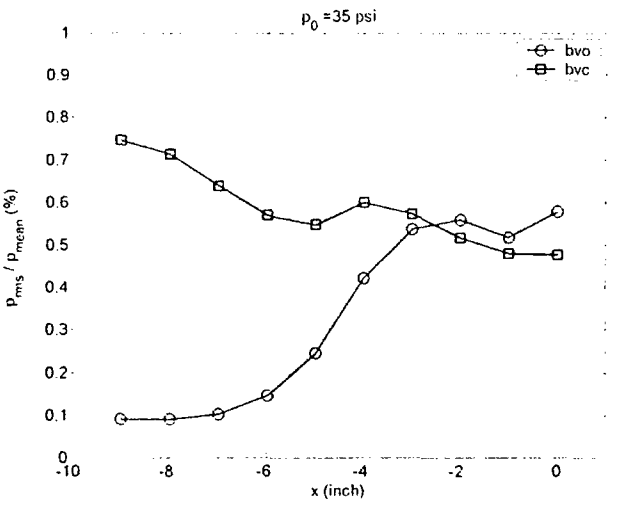

Figure A.4: Static pressure fluctuations along centerline, $p_0 = 35psi$

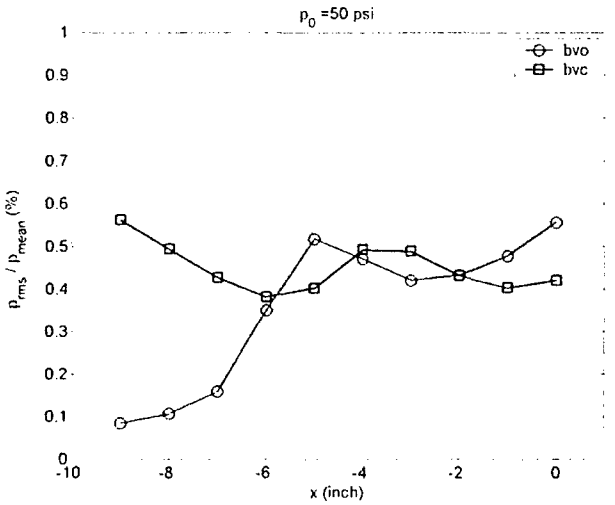

Figure A.5: Static pressure fluctuations along centerline, $p_0 = 50psi$

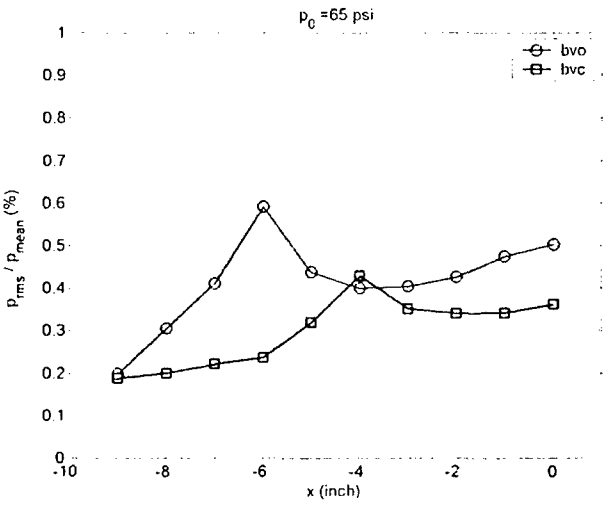

Figure A.6: Static pressure fluctuations along centerline, $p_0 = 65psi$

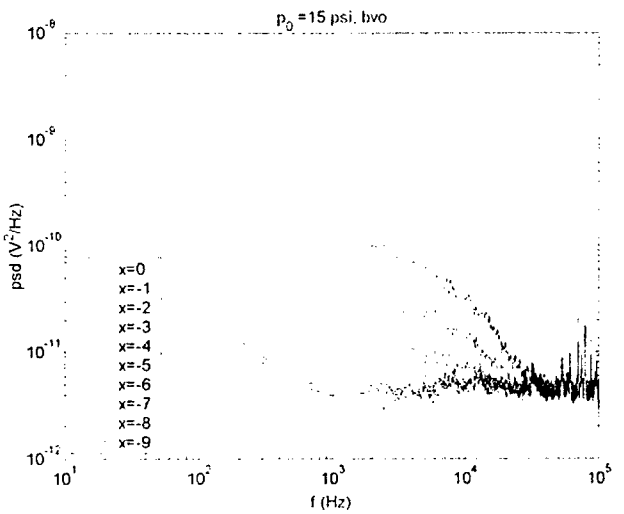

Figure A.7: PSD of free-stream disturbances, $p_0 = 15psi$, bleed valves open

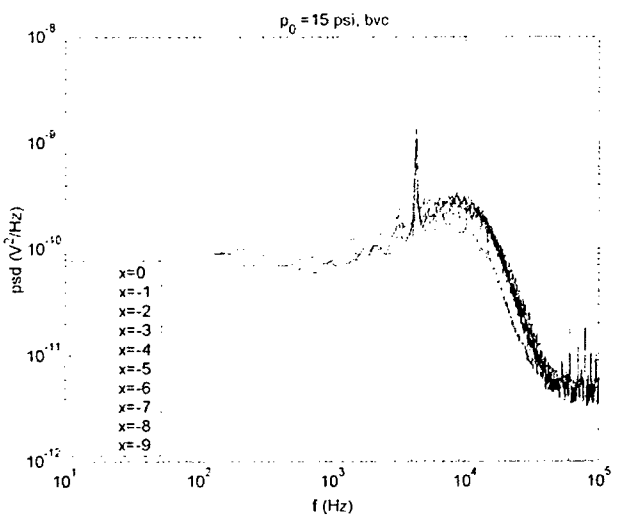

Figure A.8: PSD of free-stream disturbances, $p_0 = 15psi$, bleed valves closed

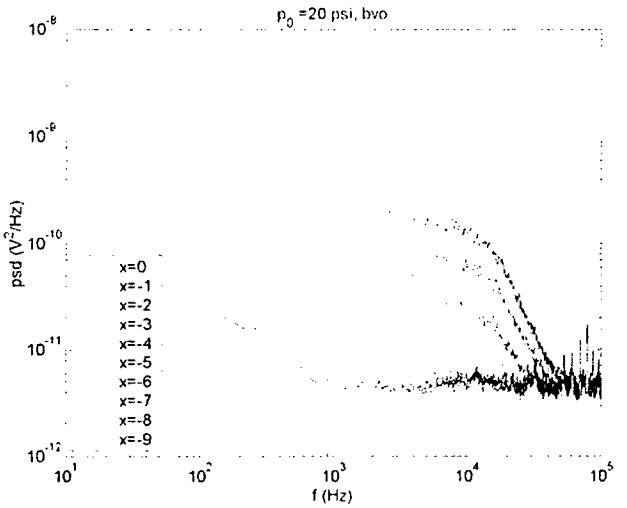

Figure A.9: PSD of free-stream disturbances, $p_0 = 20psi$, bleed valves open

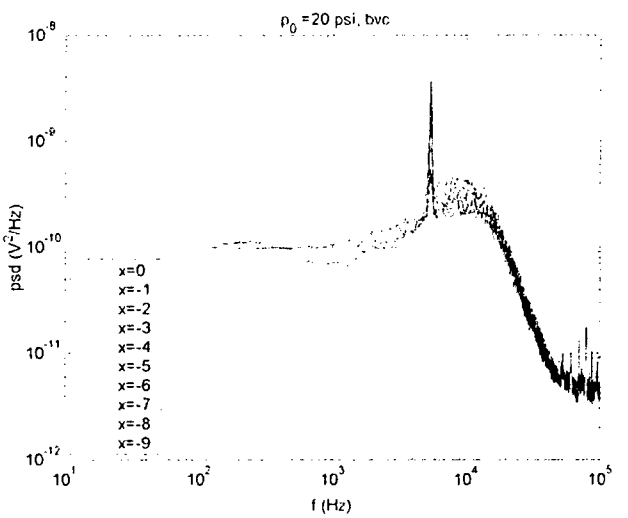

Figure A.10: PSD of free-stream disturbances, $p_0 = 20psi$, bleed valves closed

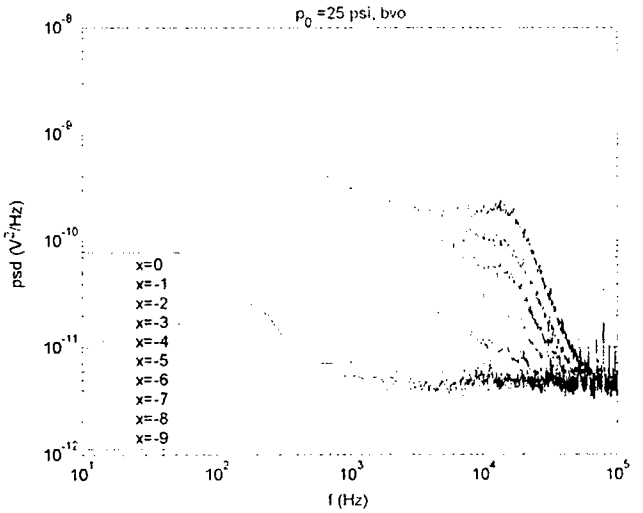

Figure A.11: PSD of free-stream disturbances, $p_0 = 25psi$, bleed valves open

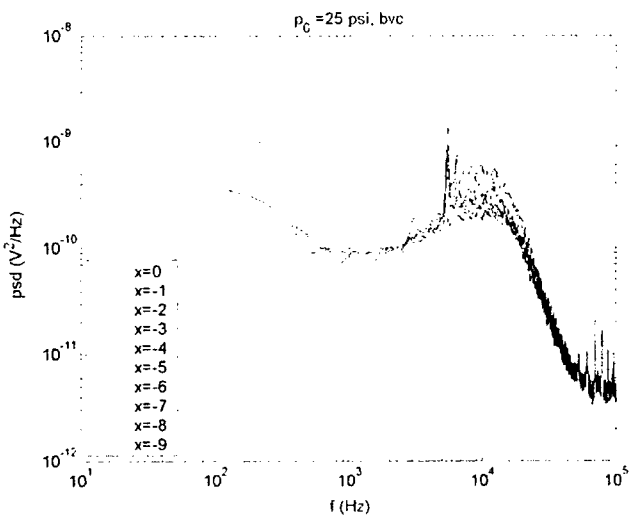

Figure A.12: PSD of free-stream disturbances, $p_0 = 25psi$, bleed valves closed

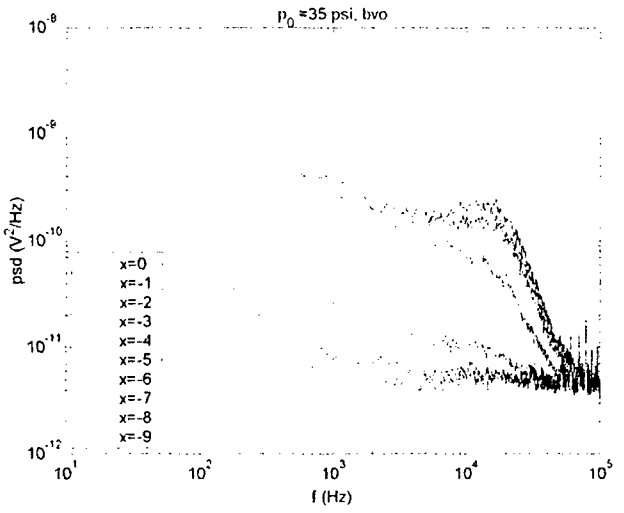

Figure A.13: PSD of free-stream disturbances, $p_0 = 35psi$, bleed valves open

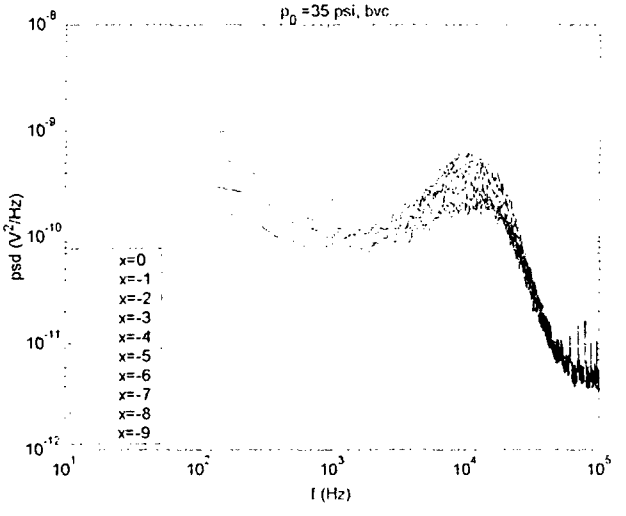

Figure A.14: PSD of free-stream disturbances, $p_0 = 35psi$, bleed valves closed

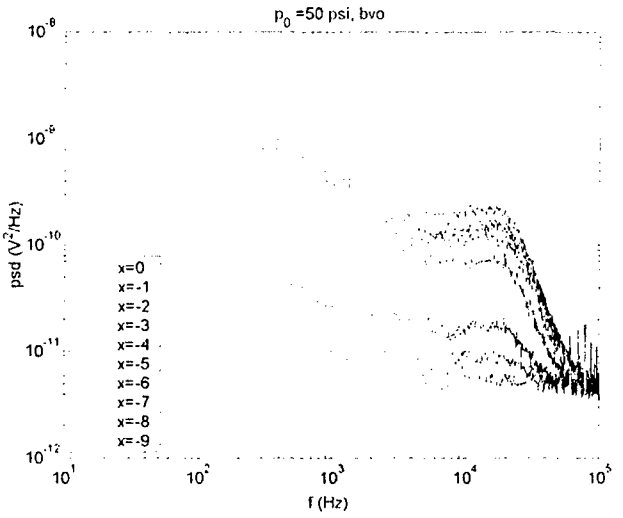

Figure A.15: PSD of free-stream disturbances, $p_0 = 50psi$, bleed valves open

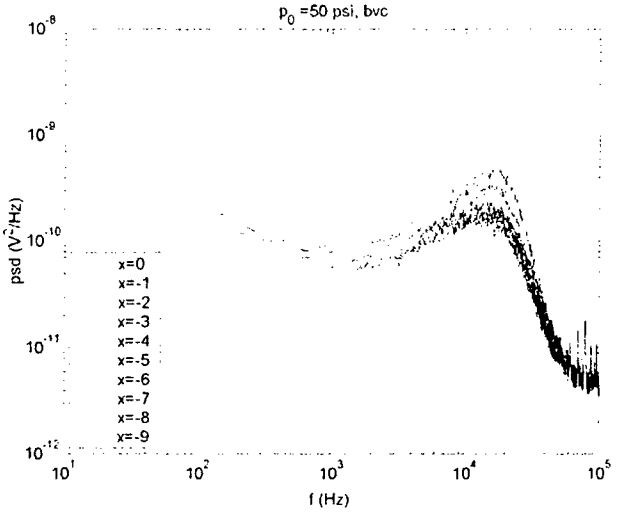

Figure A.16: PSD of free-stream disturbances, $p_0 = 50psi$, bleed valves closed

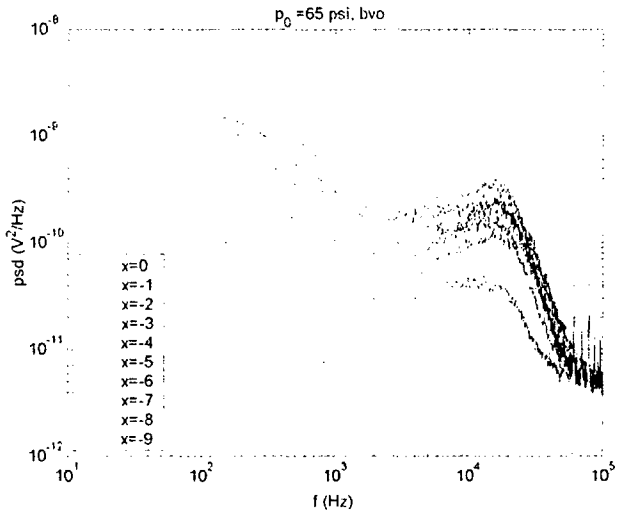

Figure A.17: PSD of free-stream disturbances, $p_0 = 65psi$, bleed valves open

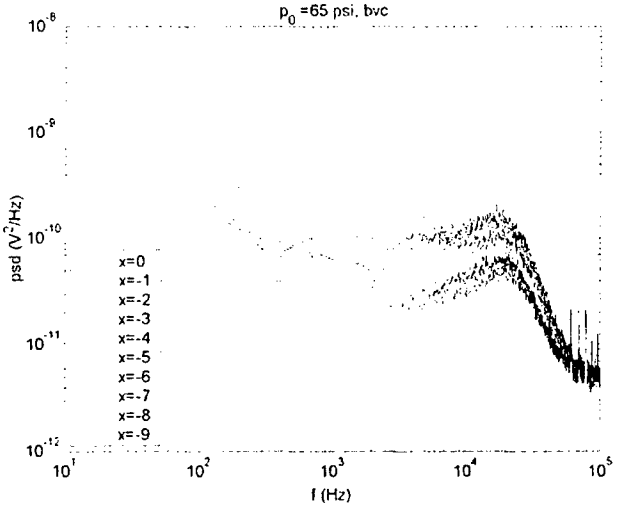

Figure A.18: PSD of free-stream disturbances, $p_0 = 65psi$, bleed valves closed

Appendix B

Mean Flow Characteristics of Incoming Boundary Layer

The mean flow properties of the incoming boundary layer are presented in this appendix. All measurements are made at $x = -0.53''$. The Pitot probe, described in Chapter 2, is used. A constant static pressure and total temperature across the boundary layer are assumed. The following profiles

- Pitot pressure profiles: $p_t/p_0(y)$
- Normalized velocity profiles: $u/u_e(y/\delta)$
- Velocity profiles in wall units: $u^+(y^+)$

at the stagnation conditions, detailed in Table 2.1, are presented.

B.1 $p_0 = 15psi$

At this stagnation pressure, the boundary layer is tripped with the *Turbulator 2.*

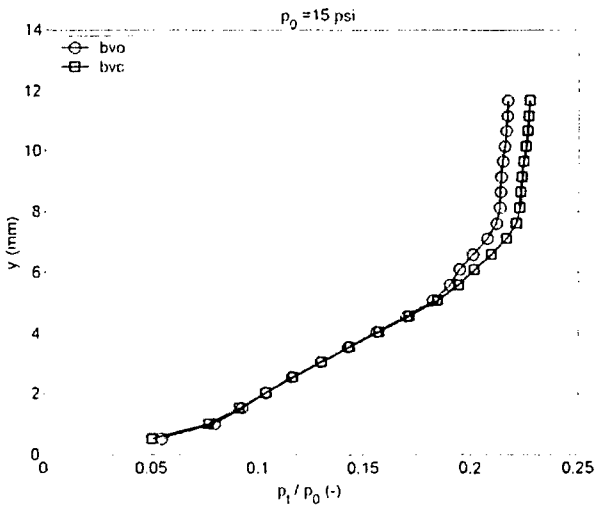

Figure B.1: Pitot pressure profiles, $p_0 = 15psi$

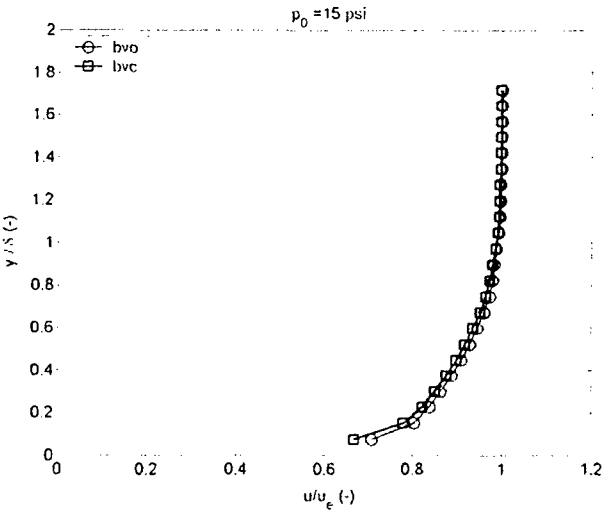

Figure B.2: Velocity profiles, $p_0 = 15psi$, $\delta = 6.8mm$

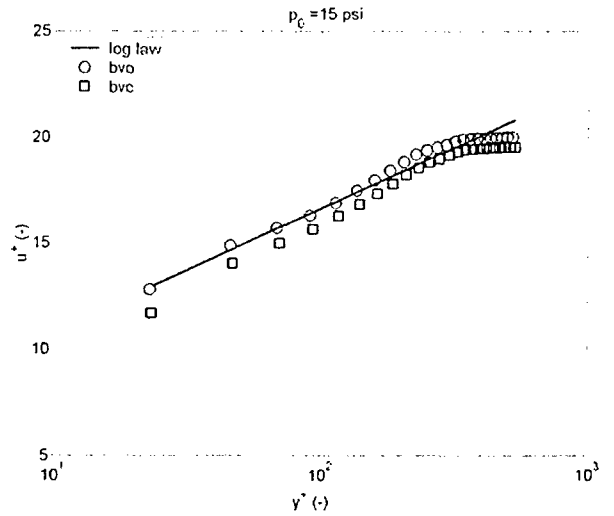

Figure B.3: Velocity profiles in wall units, $p_0 = 15psi$, $c_f = 2.15 \cdot 10^{-3}$

B.2 $p_0 = 20psi$

At this stagnation pressure, the boundary layer is tripped with the *Turbulator 2.*

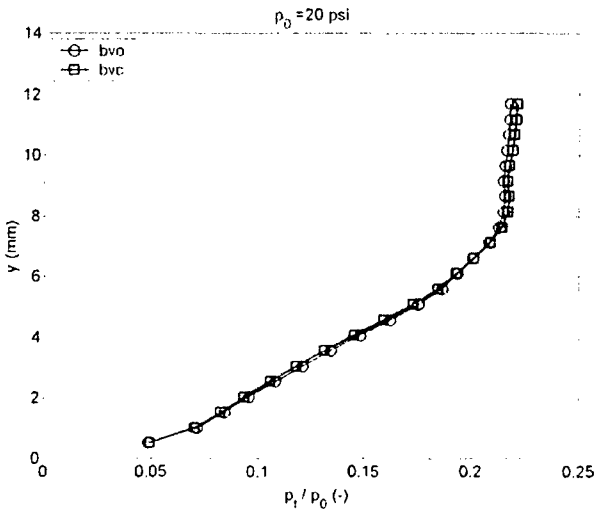

Figure B.4: Pitot pressure profiles, $p_0 = 20psi$

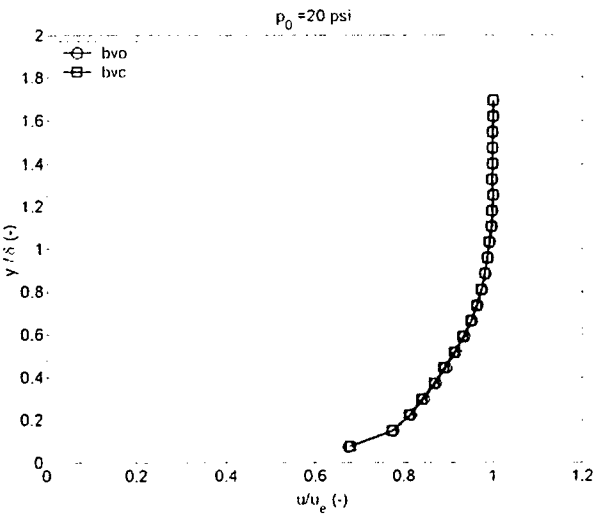

Figure B.5: Velocity profiles, $p_0 = 20psi$, $\delta = 6.9mm$

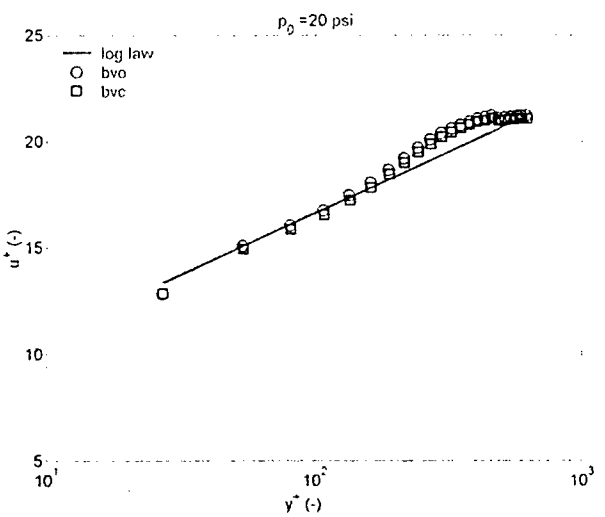

Figure B.6: Velocity profiles in wall units, $p_0 = 20psi$, $c_f = 1.95 \cdot 10^{-3}$

B.3 $p_0 = 25psi$

At this stagnation pressure, the boundary layer is tripped with the *Turbulator 2.*

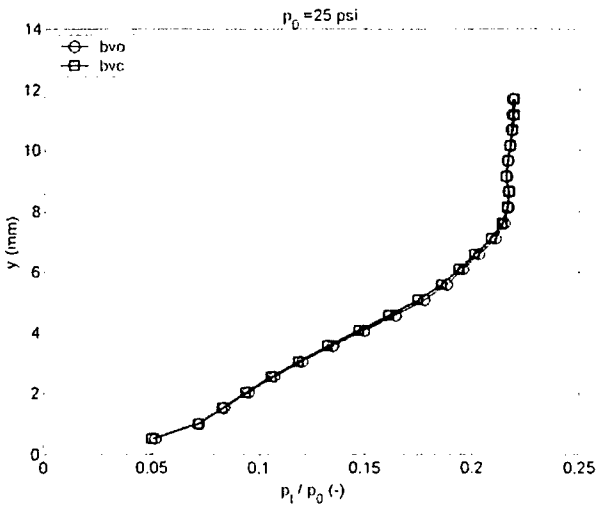

Figure B.7: Pitot pressure profiles, $p_0 = 25psi$

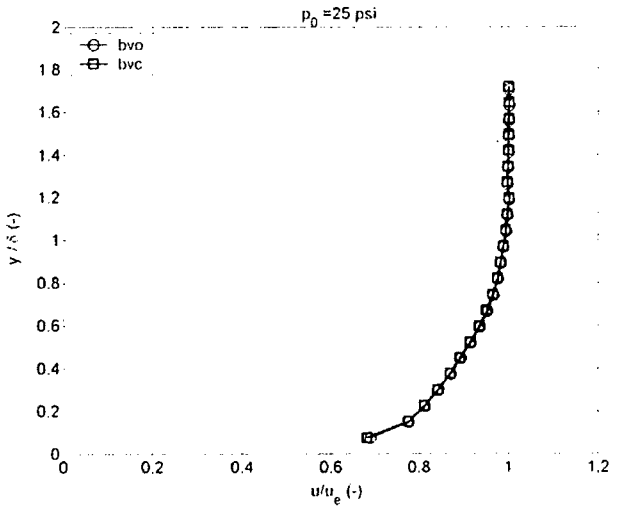

Figure B.8: Velocity profiles, $p_0 = 25psi$, $\delta = 6.85mm$

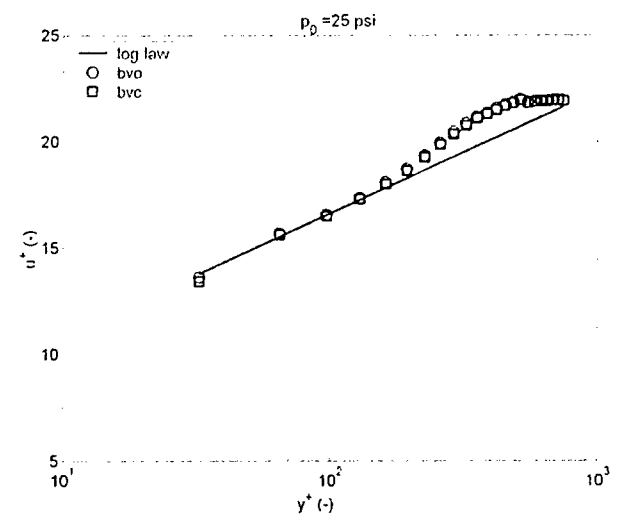

Figure B.9: Velocity profiles in wall units, $p_0 = 25psi$, $c_f = 1.82 \cdot 10^{-3}$

B.4 $p_0 = 35psi$

At this stagnation pressure, the boundary layer is tripped with the *Turbulator 2.*

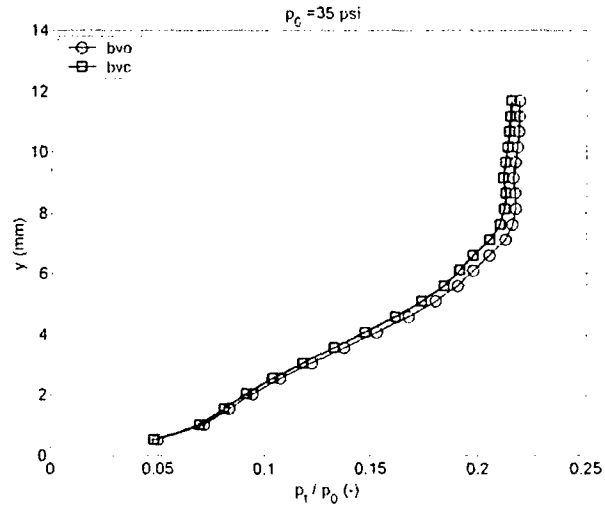

Figure B.10: Pitot pressure profiles, $p_0 = 35psi$

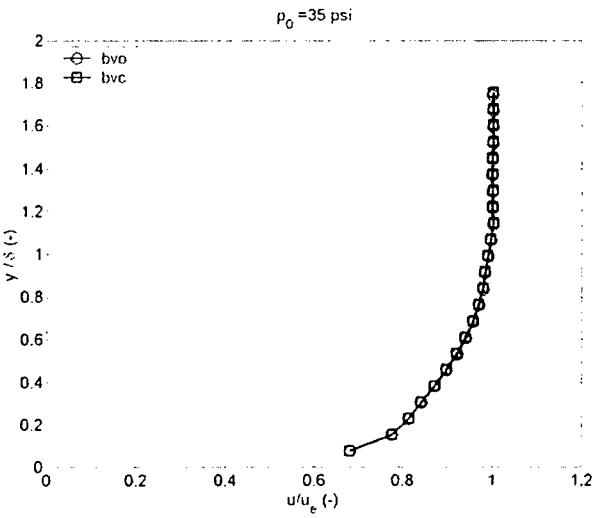

Figure B.11: Velocity profiles, $p_0 = 35psi$, $\delta = 6.70mm$

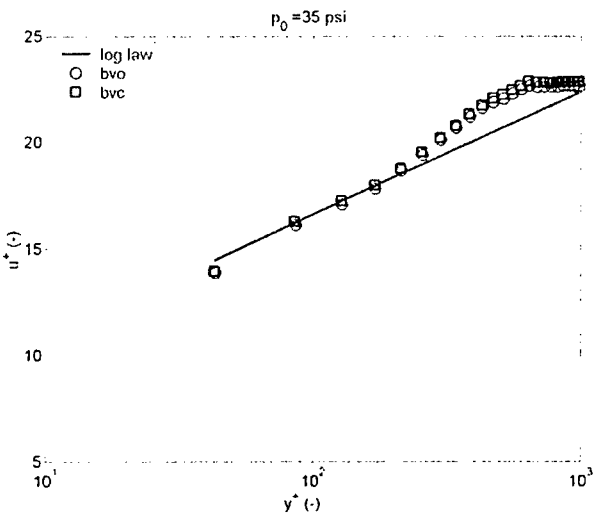

Figure B.12: Velocity profiles in wall units, $p_0 = 35psi$, $c_f = 1.70 \cdot 10^{-3}$

B.5 $p_0 = 50psi$

At this stagnation pressure, the boundary layer is tripped with the *Turbulator 1.*

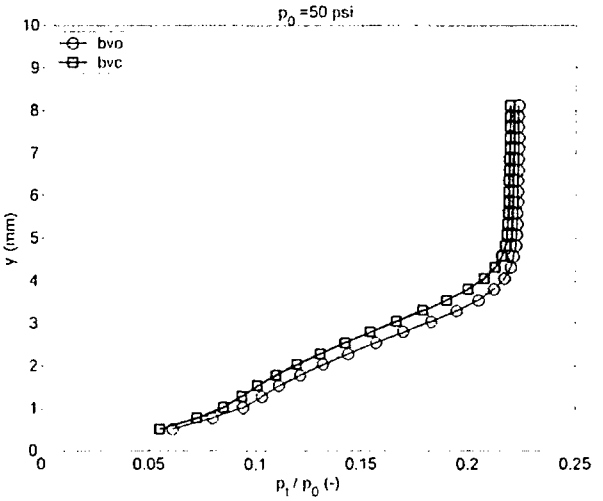

Figure B.13: Pitot pressure profiles, $p_0 = 50psi$

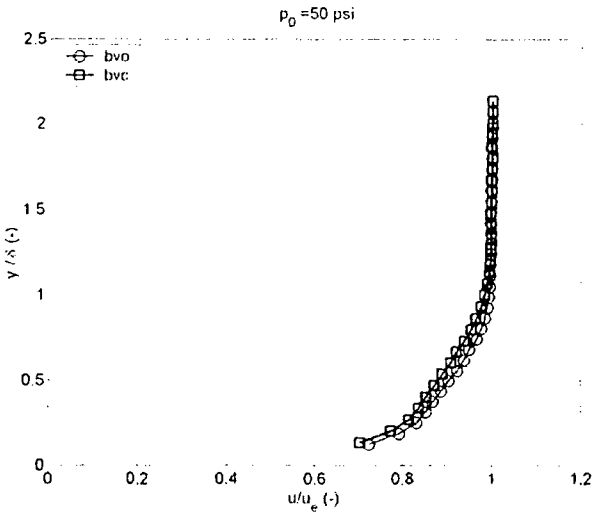

Figure B.14: Velocity profiles, $p_0 = 50psi$, $\delta_{bvc} = 4.1mm$, $\delta_{bvo} = 3.8mm$

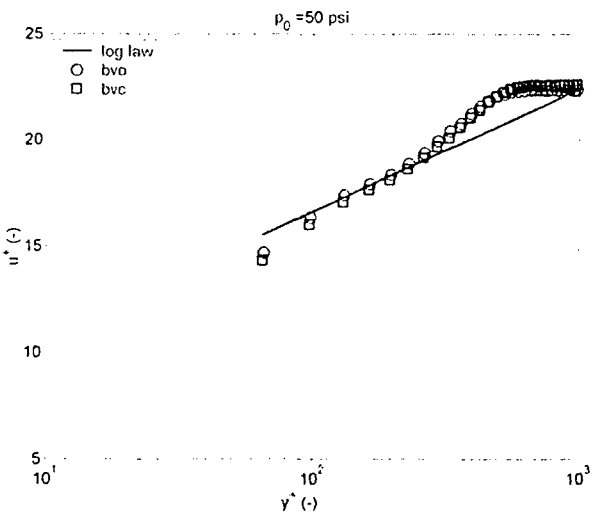

Figure B.15: Velocity profiles in wall units, $p_0 = 50psi$, $c_f = 1.72 \cdot 10^{-3}$

B.6 $p_0 = 65psi$

At this stagnation pressure, the boundary layer is tripped with the *Turbulator 1.*

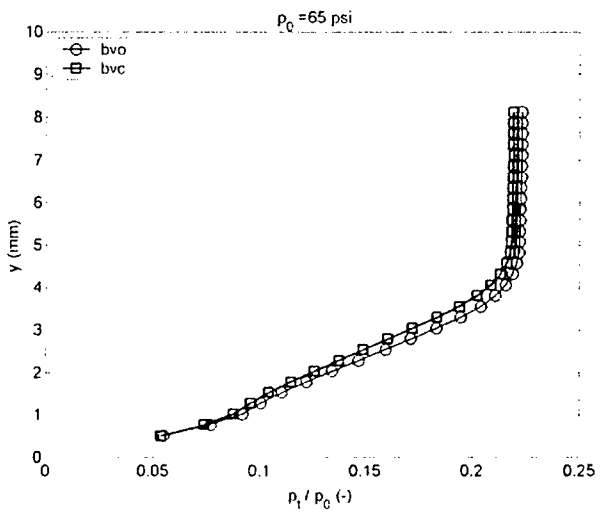

Figure B.16: Pitot pressure profiles, $p_0 = 65psi$

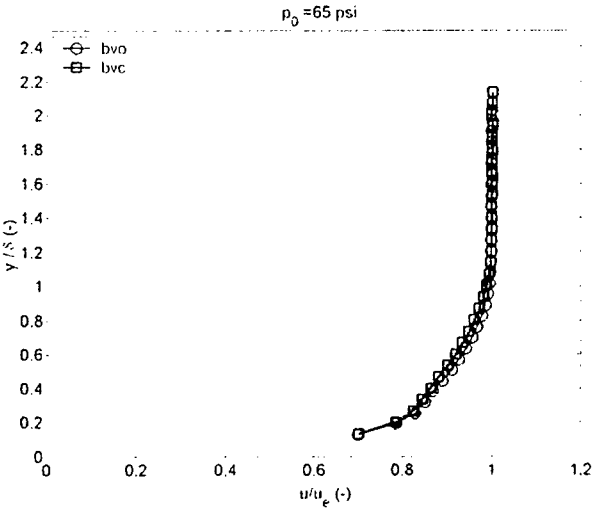

Figure B.17: Velocity profiles, $p_0 = 65psi$, $\delta_{bvc} = 4.0mm$, $\delta_{bvo} = 3.8mm$

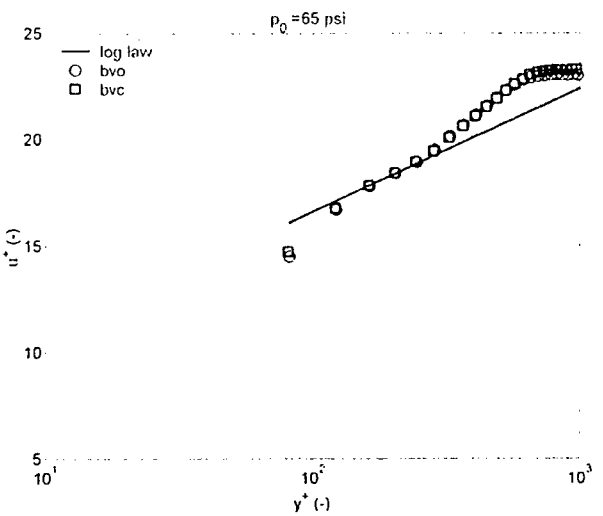

Figure B.18: Velocity profiles in wall units, $p_0 = 65psi$, $c_f = 1.62 \cdot 10^{-3}$

Appendix C

Fluctuating Characteristics of Incoming Boundary Layer

The fluctuating flow properties of the incoming boundary layer are presented in this appendix. All measurements were taken at one station $x = -0.53''$ upstream of the ramp corner location. The data was obtained using a single hot-wire probe operated at an overheat of $a_w = 0.8$. It was assumed that the probe is only sensitive to the longitudinal mass flow ρu.

Profiles of the relative mass flow fluctuation $(\rho u)_{rms}/\overline{\rho u}$ are presented for each stagnation conditions (Table 2.1). The spectra of the anemometer output at $y/\delta \simeq 0.5$, which correspond to the maximum level of fluctuations in the boundary layer, are also presented.

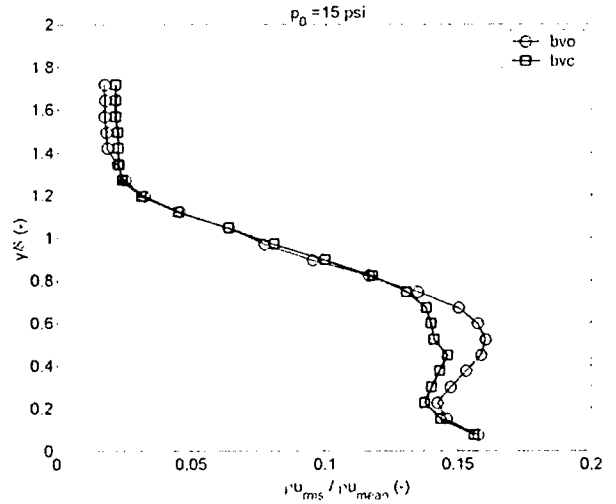

Figure C.1: Fluctuating mass flow profiles, $p_0 = 15psi$

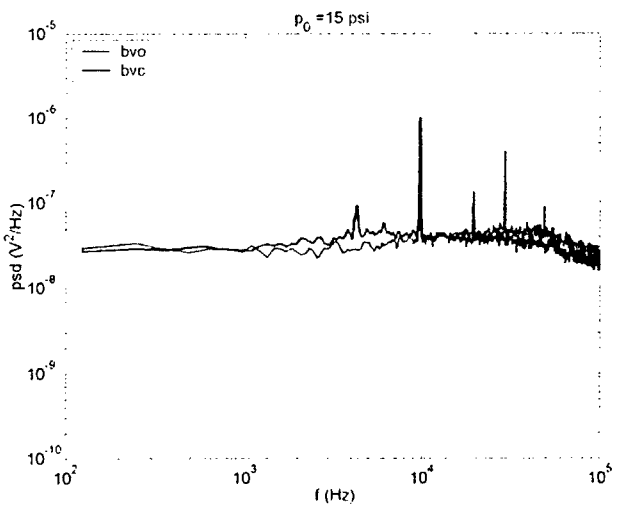

Figure C.2: Spectra of anemometer output voltage, $y/\delta \simeq 0.5$, $p_0 = 15psi$

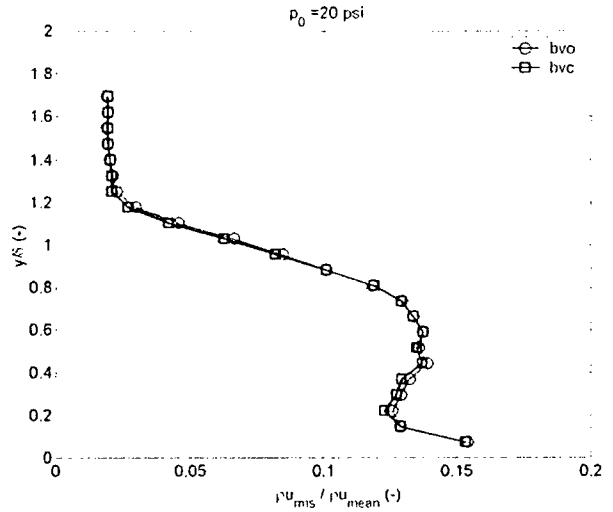

Figure C.3: Fluctuating mass flow profiles, $p_0 = 20psi$

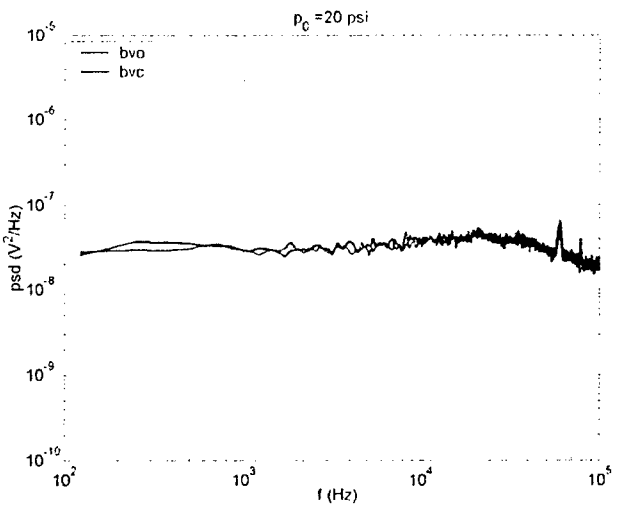

Figure C.4: Spectra of anemometer output voltage, $y/\delta \simeq 0.5$, $p_0 = 20psi$

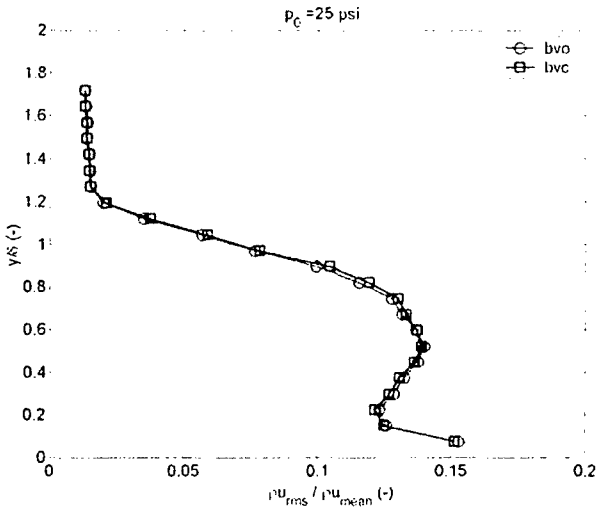

Figure C.5: Fluctuating mass flow profiles, $p_0 = 25psi$

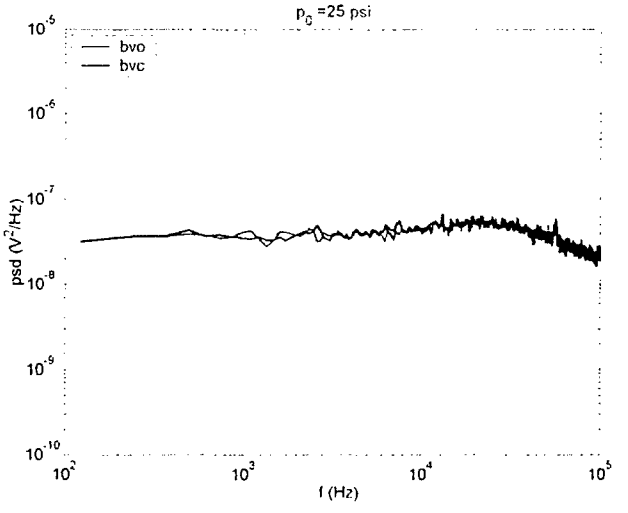

Figure C.6: Spectra of anemometer output voltage, $y/\delta \simeq 0.5$, $p_0 = 25psi$

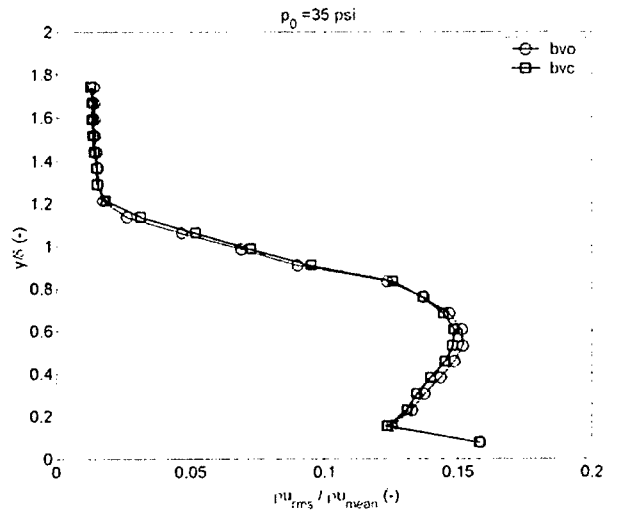

Figure C.7: Fluctuating mass flow profiles, $p_0 = 35psi$

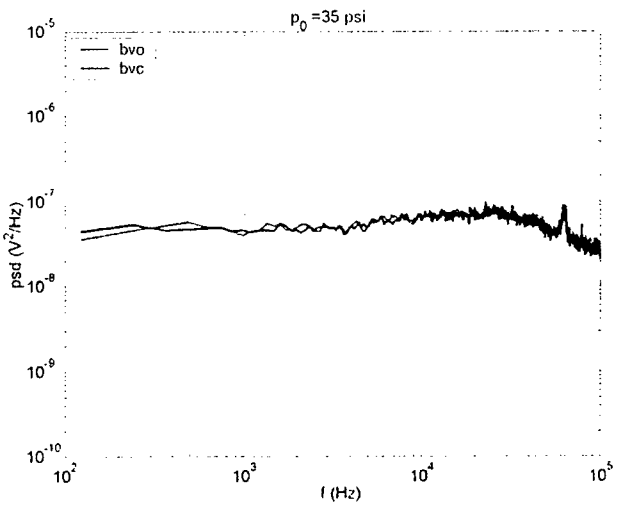

Figure C.8: Spectra of anemometer output voltage, $y/\delta \simeq 0.5$, $p_0 = 35psi$

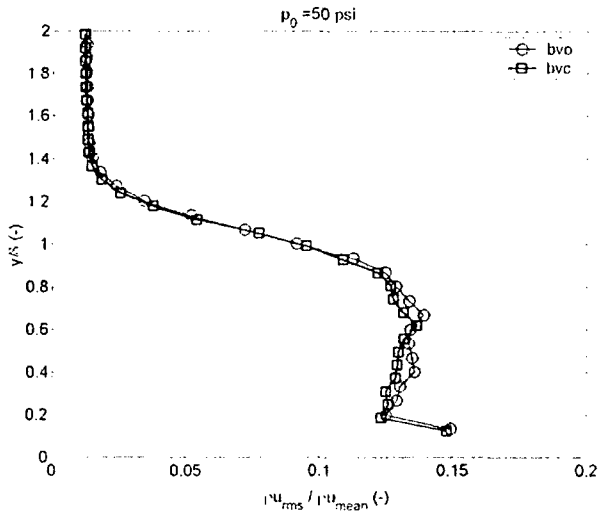

Figure C.9: Fluctuating mass flow profiles, $p_0 = 50psi$

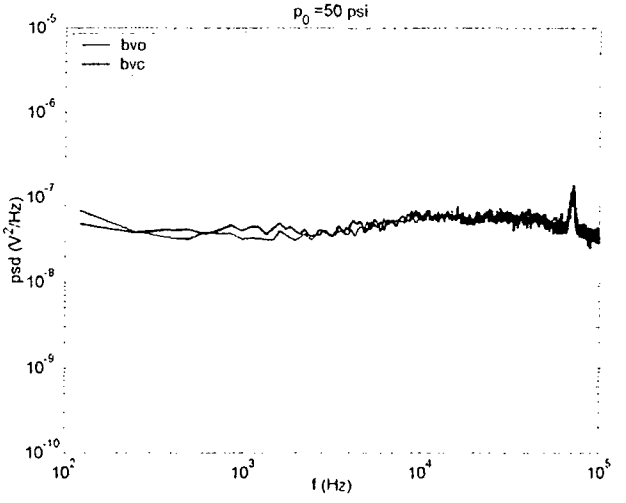

Figure C.10: Spectra of anemometer output voltage, $y/\delta \simeq 0.5$, $p_0 = 50psi$

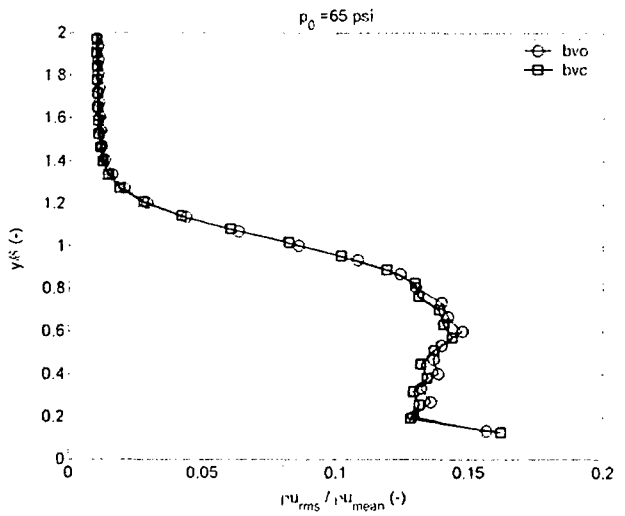

Figure C.11: Fluctuating mass flow profiles, $p_0 = 65psi$

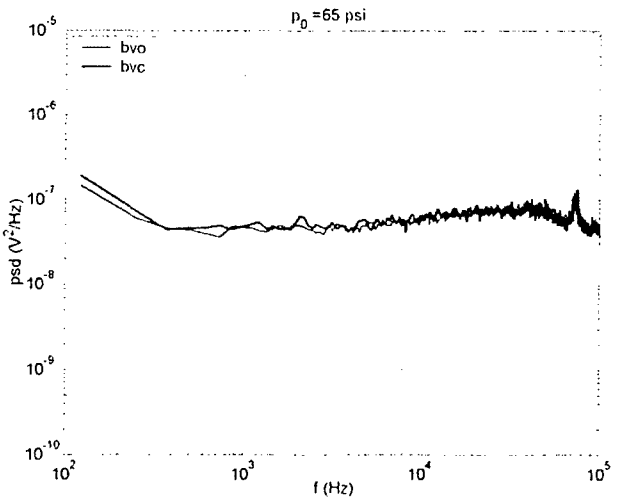

Figure C.12: Spectra of anemometer output voltage, $y/\delta \simeq 0.5$, $p_0 = 65psi$

Appendix D

Schlieren Images of the Interaction

Instantaneous focusing schlieren images of the flow over the compression ramp are presented in this appendix. The images are obtained using 50% cut-off. (As no image was taken at $p_0 = 65psi$, an image for $p_0 = 75psi$ is shown.) The height of the incoming boundary layer thickness is shown in each image.

Figure D.1: Schlieren image of STBLI, $p_0 = 15psi$, BVC

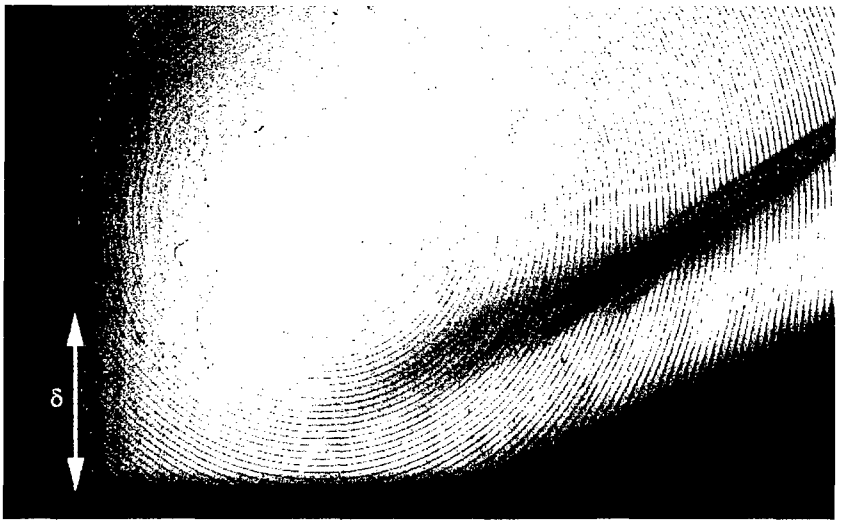

Figure D.2: Schlieren image of STBLI, $p_0 = 15psi$, BVO

Figure D.3: Schlieren image of STBLI, $p_0 = 20psi$, BVC

Figure D.4: Schlieren image of STBLI, $p_0 = 20psi$, BVO

Figure D.5: Schlieren image of STBLI, $p_0 = 25psi$, BVC

Figure D.6: Schlieren image of STBLI, $p_0 = 25psi$, BVO

Figure D.7: Schlieren image of STBLI, $p_0 = 35psi$, BVC

Figure D.8: Schlieren image of STBLI, $p_0 = 35psi$, BVO

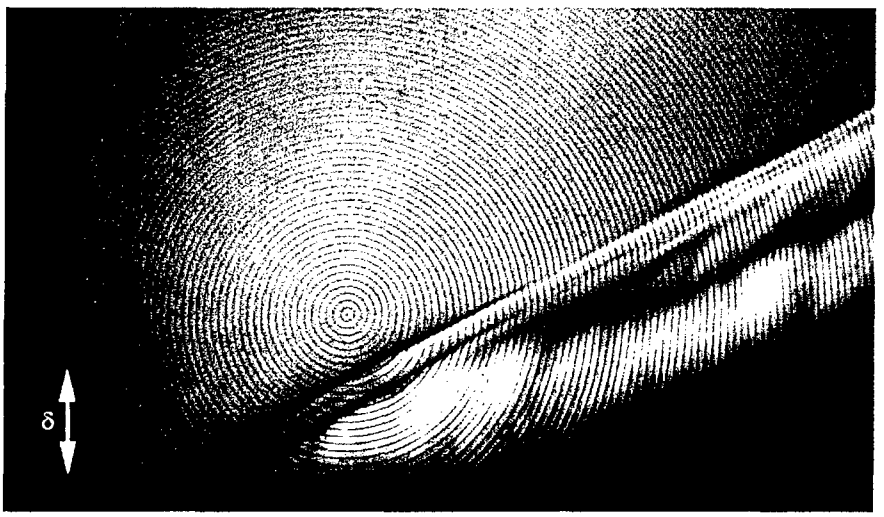

Figure D.9: Schlieren image of STBLI, $p_0 = 50psi$, BVC

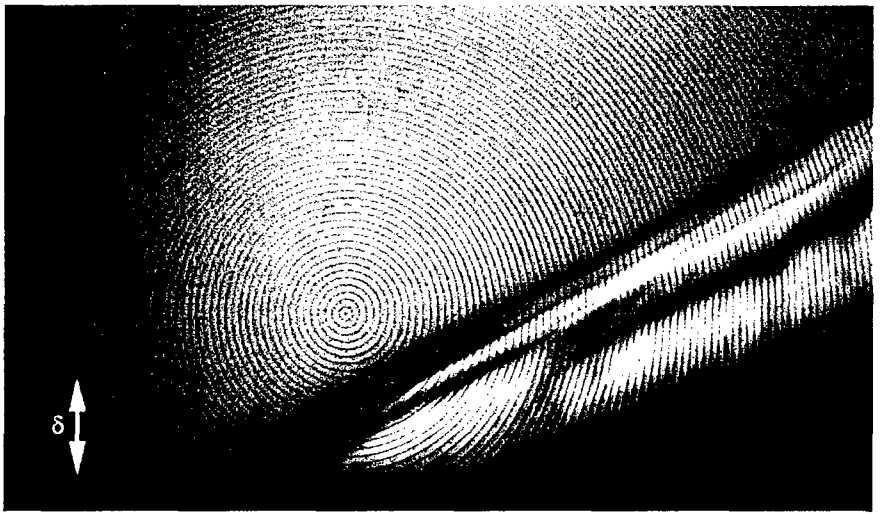

Figure D.10: Schlieren image of STBLI, $p_0 = 50psi$, BVO

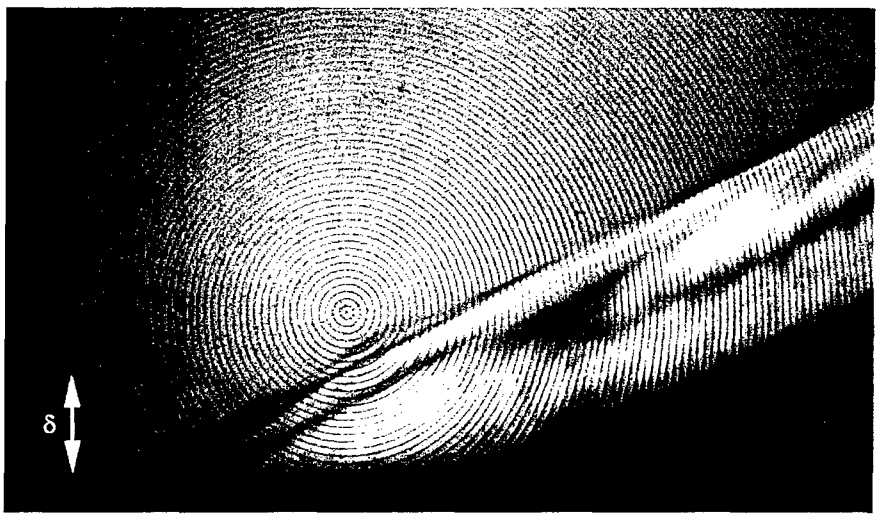

Figure D.11: Schlieren image of STBLI, $p_0 = 75psi$, BVC

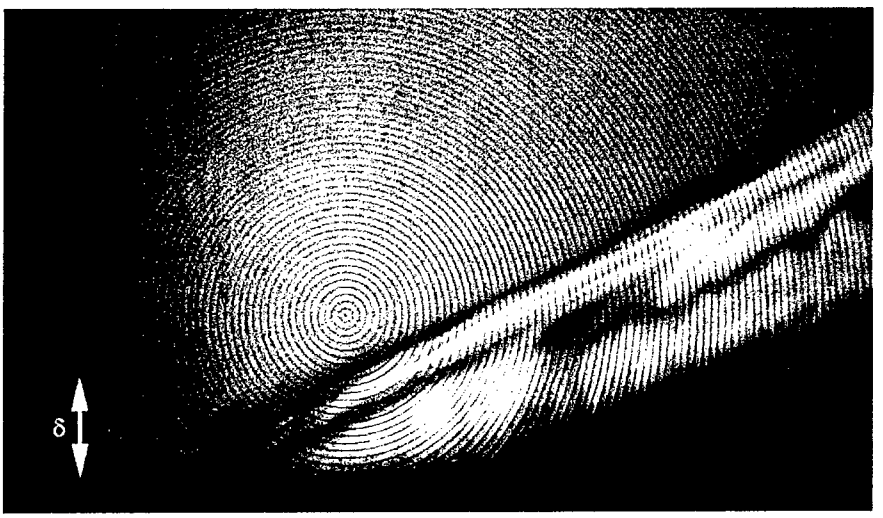

Figure D.12: Schlieren image of STBLI, $p_0 = 75psi$, BVO

Appendix E

Unsteady Characteristics of STBLI

Results of the hot-film surveys are presented in this appendix. The cylindrical hot-film is positioned at $y = 1.5\delta$ and, as described in section 2.3.5, is traversed streamwise across the separation shock wave. The figures below show the variation of the mass flow RMS normalized by the mass flow value upstream of the shock. The origin $x = 0$ is chosen arbitrarily *for each stagnation pressure.* Thus, a comparison of the relative shock locations is valid only for a given plot. In each plot, x is normalized by the incoming boundary layer thickness δ.

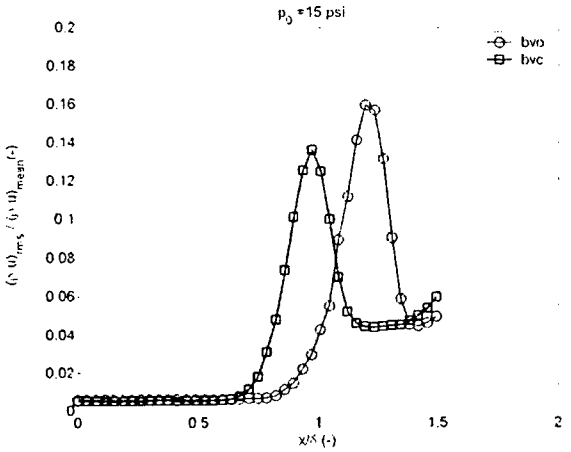

Figure E.1: RMS of mass flow fluctuations across shock, $p_0 = 15psi$, $\delta = 6.8mm$

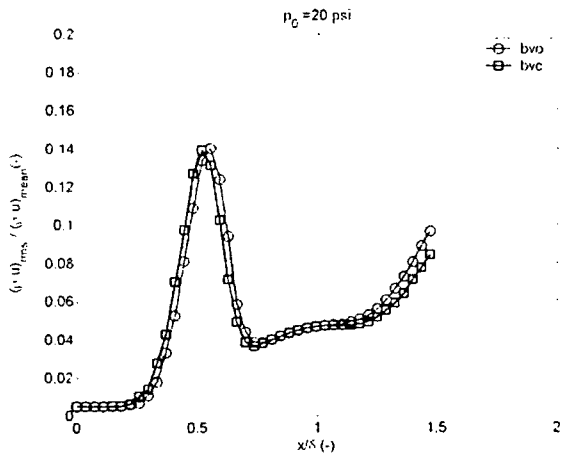

Figure E.2: RMS of mass flow fluctuations across shock, $p_0 = 20psi$, $\delta = 6.9mm$

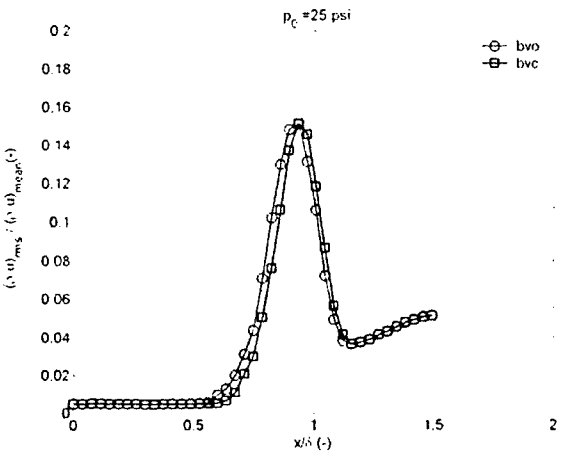

Figure E.3: RMS of mass flow fluctuations across shock, $p_0 = 25psi$, $\delta = 6.8mm$

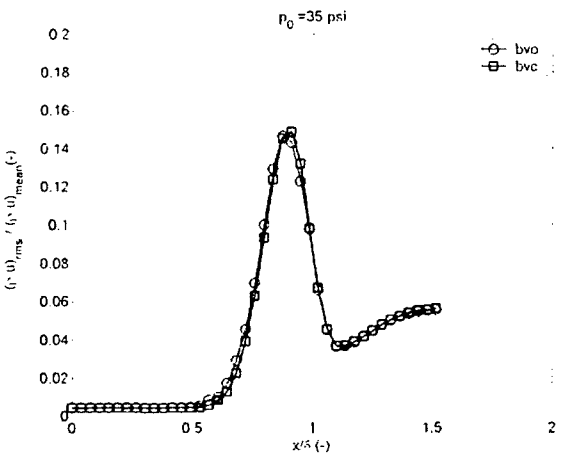

Figure E.4: RMS of mass flow fluctuations across shock, $p_0 = 35psi$, $\delta = 6.7mm$

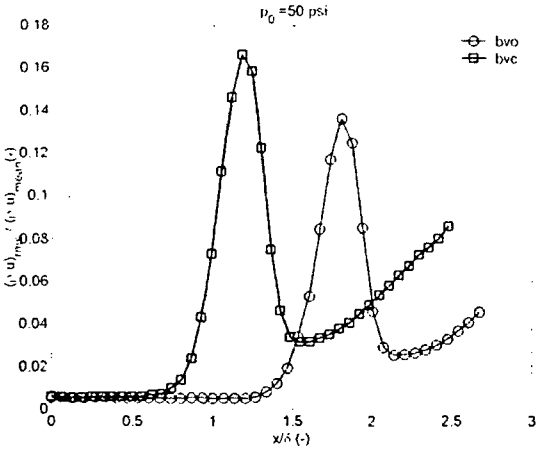

Figure E.5: RMS of mass flow fluctuations across shock, $p_0 = 50psi$, $\delta_{bvc} = 4.1mm$, $\delta_{bvo} = 3.8mm$

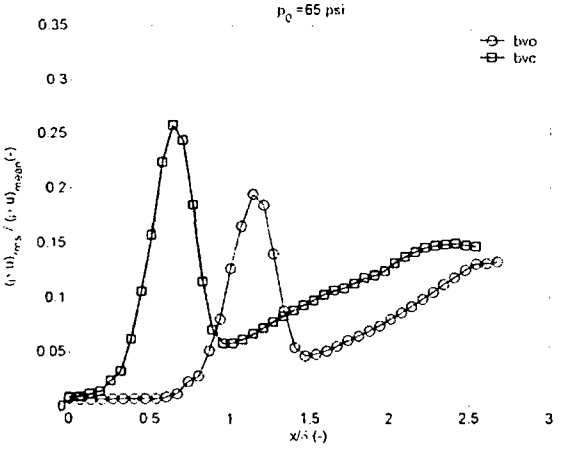

Figure E.6: RMS of mass flow fluctuations across shock, $p_0 = 65psi$, $\delta_{bvc} = 4.0mm$, $\delta_{bvo} = 3.8mm$